Enhancing the longevity of magnesium implants with cold-sprayed Ta/Ag coatings: Optimization of corrosion and wear resistance

Original
Enhancing the longevity of magnesium implants with cold-sprayed Ta/Ag coatings: Optimization of corrosion and wear resistance / Yu, Pengfei; Sheibanian, Nazanin; Perumal, Gopinath; Sesana, Raffaella; Brabazon, Dermot; Xie, Yingchun; Yin, Shuo; Lupoi, Rocco. - In: JOURNAL OF MATERIALS RESEARCH AND TECHNOLOGY. - ISSN 2238-7854. - ELETTRONICO. - 35:(2025), pp. 7235-7252. [10.1016/j.jmrt.2025.03.048]

Publisher:
Elsevier

Published
DOI:10.1016/j.jmrt.2025.03.048

Journal of Materials Research and Technology 35 (2025) 7235–7252

Contents lists available at ScienceDirect

Journal of Materials Research and Technology

journal homepage: www.elsevier.com/locate/jmrt

Enhancing the longevity of magnesium implants with cold-sprayed Ta/Ag coatings: Optimization of corrosion and wear resistance

Pengfei Yu [a,*], Nazanin Sheibanian [b,c], Gopinath Perumal [c], Raffaella Sesana [b], Dermot Brabazon [d], Yingchun Xie [e], Shuo Yin [a], Rocco Lupoi [a,**]

[a] Department of Mechanical, Manufacturing and Biomedical Engineering, Trinity College Dublin, The University of Dublin, Parsons Building, Dublin 2, Ireland
[b] Department of Mechanical and Aerospace Engineering, Politecnico di Torino, Corso Duca degli Abruzzi 24, 10129, Torino, Italy
[c] TSUBAKI NAKASHIMA Central Laboratory (TN ITALY), Corso Torino 378, Pinerolo, 10064, Torino, Italy
[d] I-Form Advanced Manufacturing Research Centre, Dublin City University, Dublin, Ireland
[e] Institute of New Materials, Guangdong Academy of Sciences, National Engineering Laboratory of Modern Materials Surface Engineering Technology, Guangdong Provincial Key Laboratory of Modern Surface Engineering Technology, Guangzhou, 510651, China

ARTICLE INFO

Handling editor: P.Y. Chen

Keywords:
Cold spray
Tantalum/Ag composites
Magnesium alloys
Corrosion resistance
Wear performance

ABSTRACT

Magnesium alloys are gaining attention for biomedical implants due to their lightweight nature and bone-mimicking mechanical properties. However, their high reactivity and vulnerability to corrosion restrict their long-term application in biomedicine. This study explores the potential of enhancing corrosion resistance and wear performance of magnesium through tantalum/silver (Ta/Ag) composite coatings manufactured by cold spray for durable implant devices. The coatings exhibited adhesive strengths ranging from 22.5 to 27.5 MPa, sufficient to prevent delamination. The inclusion of silver in the composites effectively protected the tantalum matrix from corrosion, preserving its structural integrity over a long period of corrosion. Additionally, a higher silver content improved fatigue wear resistance by inhibiting crack propagation and increased the hardness-to-Young's modulus ratio through in-situ mechanical mixing of Ag and Ta during wear, which also reduced the generation of free debris particles. Among the tested compositions, the Ta–5Ag composite offered the best overall protection, optimizing corrosion resistance, wear performance, and mechanical stability. These results indicate that cold sprayed Ta/Ag composite coatings are a promising approach to making magnesium alloys more viable as long-term implant materials.

1. Introduction

Magnesium alloys, recognized for their low density and excellent mechanical properties, are highly regarded for lightweight structural applications. Recently, their mechanical similarity to human bone has made them increasingly popular in the field of metallic implants [1,2]. Unlike titanium and cobalt-chromium alloys, magnesium is not only essential for various physiological processes but can also be easily metabolized and excreted by the body, offering superior biocompatibility and biosafety [3]. However, the high reactivity of Magnesium, particularly its susceptibility to corrosion in humid environments, poses significant challenges [4]. While the formation of a dense oxide film on magnesium can provide some protection in dry conditions, this film deteriorates in moisture and aqueous, accelerating corrosion process [5]. This susceptibility to corrosion limits the use of magnesium alloys in structural applications but also makes them a promising option for biodegradable implants [6]. Devices, such as screws and fixation plates, could eliminate the need for secondary surgeries, simplifying treatment and reducing patient discomfort. Magnesium alloys also show potential in the development of biodegradable vascular stents, with research already underway [7]. Nevertheless, the same rapid corrosion that makes magnesium alloys suitable for biodegradable implants also presents clinical complications. In bodily fluids, the protective oxide film on magnesium alloys can be easily compromised, leading to accelerated corrosion. This process generates magnesium hydroxide and hydrogen gas, which can accumulate in the body, potentially causing inflammation and jeopardizing surgical outcomes [8,9]. Moreover, the high corrosion rate limits the use of magnesium alloys for long-term or

---

* Corresponding author.
** Corresponding author.
E-mail addresses: yup1@tcd.ie (P. Yu), LUPOIR@tcd.ie (R. Lupoi).

https://doi.org/10.1016/j.jmrt.2025.03.048
Received 23 January 2025; Received in revised form 27 February 2025; Accepted 6 March 2025

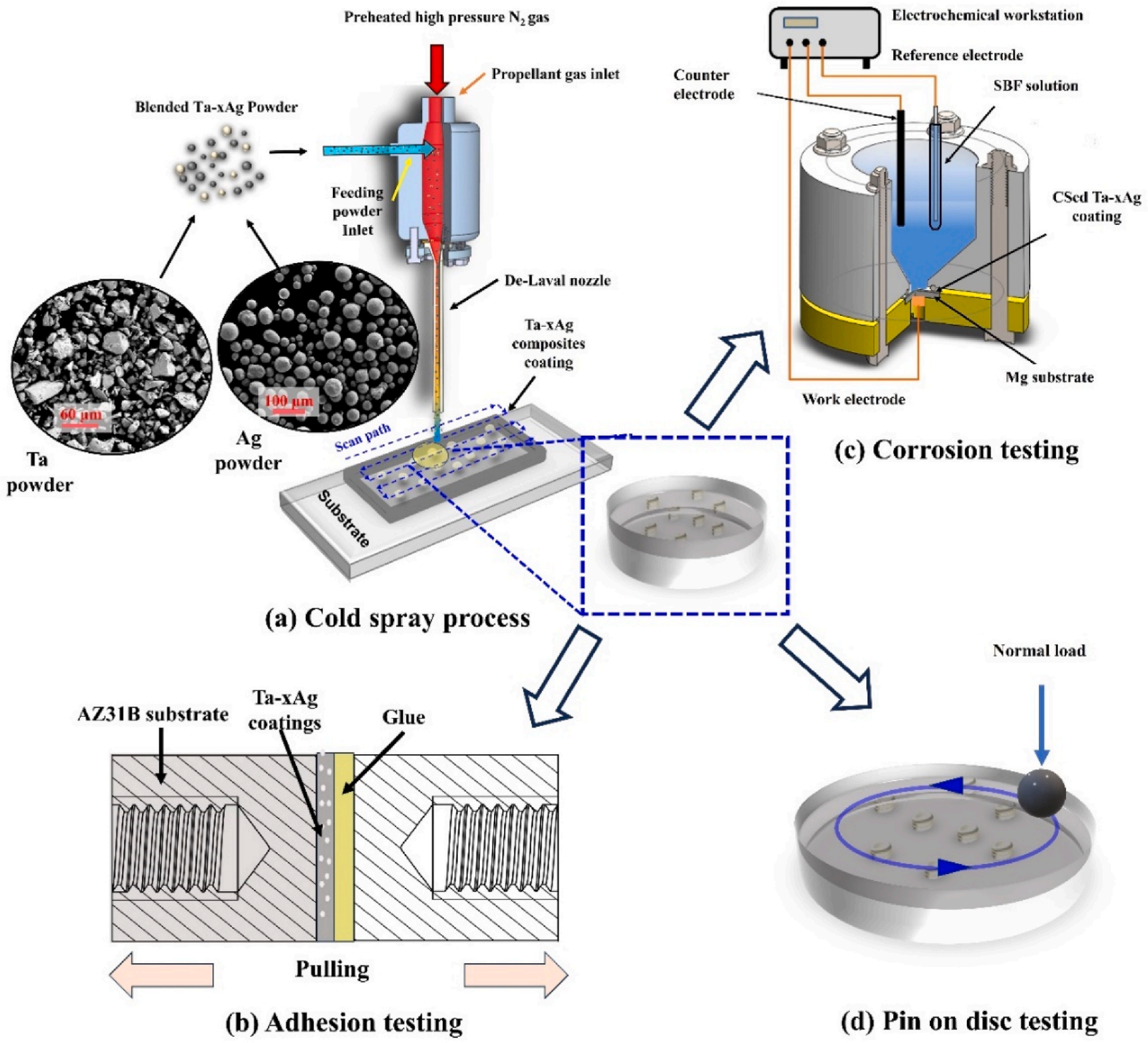

Fig. 1. Schematic of cold spray and testing procedure.

Table 1
Constitution of SBF solution used in the corrosion testing.

Ion	Concentration (mol·m^{-3})	
	SBF	Blood Plasma
Na^+	142.0	142.0
K^+	5.0	5.0
Mg^{2+}	1.5	1.5
Ca^{2+}	2.5	2.5
Cl^-	103.0	103.0
HCO_3^-	10.0	27.0
HPO_4^{2-}	1.0	1.0
SO_4^{2-}	0.5	0.5

permanent implants that are essential for trauma repair or plastic surgery, preventing full utilisation of their lightweight and mechanical benefits.

To slow down the corrosion of magnesium alloys, two primary strategies are currently employed: adjusting the alloy composition and applying surface modifications [10–14]. Among these, surface modification, particularly through the use of protective coatings, stands out as an effective approach [12–17]. Unlike alloy composition adjustments, protective coatings can shield magnesium from corrosive environments without altering its mechanical properties, thus extending the service life of magnesium components. Inorganic non-metallic and organic coatings are commonly used for this purpose, fabricated via techniques such as chemical conversion, surface anodization, and physical or chemical vapour deposition (PVD/CVD) [15,18–21]. However, these coatings often face challenges such as low adhesion, poor wear resistance and low fatigue life, which may result in unexpected failure in the complex mechanical working conditions in human body characterized by constant and cyclic load [8,22]. Additionally, some of these processes involve toxic chemicals or require sophisticated equipment and processes, resulting in both high environmental and economic costs. In contrast, metallic coatings possess superior strength and ductility, making them more compatible with the magnesium substrate [23–26]. These coatings typically provide better adhesion, wear resistance, and fatigue resistance. However, because magnesium alloys have a more negative electrochemical potential than most metals, any damage to the coating can result in galvanic corrosion, significantly accelerating the degradation of the underlying magnesium alloy. Additionally, the cyclic load leads to small oscillatory motion between tissue and implant surface, often resulting in fatigue wear damage. The wear particles can be recognized as aliens by immune system, inducing a severe inflammatory response [27]. To maximize the effectiveness of metallic coatings while minimizing the risk of galvanic corrosion, the coating must be dense and exhibit excellent corrosion and fatigue wear resistance.

Thermal spray is one of effective technique that has been extensively

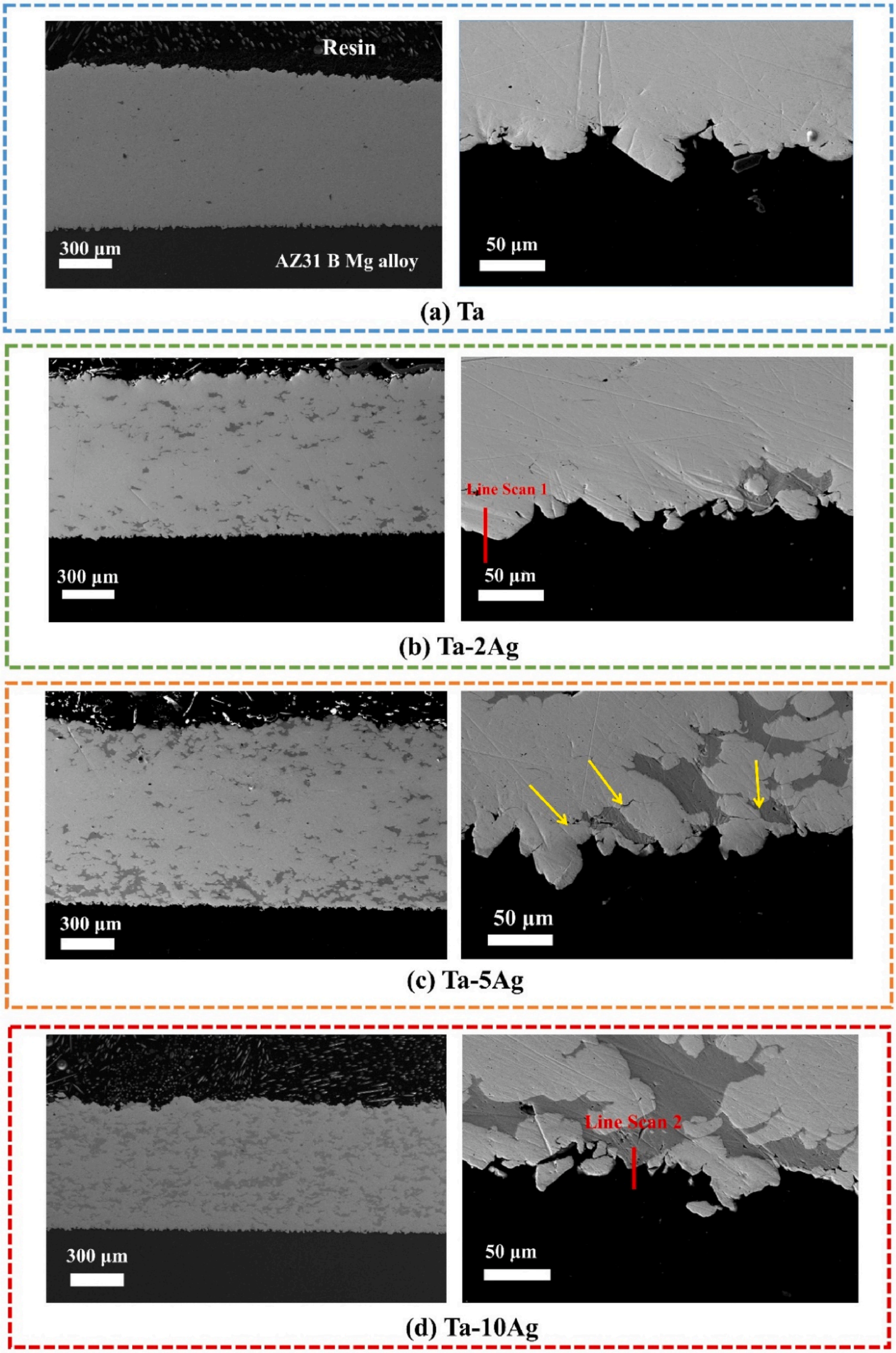

Fig. 2. Cross-section microstructure of cold sprayed Ta and Ta-xAg composites coating. (a) pure Ta, (b) Ta–2Ag, (c) Ta–5Ag, (d) Ta–10Ag.

used to apply coatings on various metal surfaces [16–18]. However, the high processing temperatures inherent in thermal spraying can lead to significant oxidation of reactive magnesium (Mg) substrates, which in turn results in poor bonding between the coating and the substrate. Moreover, the thermal residual stresses induced by the process can cause delamination of the coatings [19]. In contrast, cold spray technology (CS) operates at low processing temperatures, effectively mitigating the adverse effects associated with high thermal input. In the CS process, feedstock powders are fed into a high-pressure heated gas stream and accelerated to extremely high velocities as they pass through a

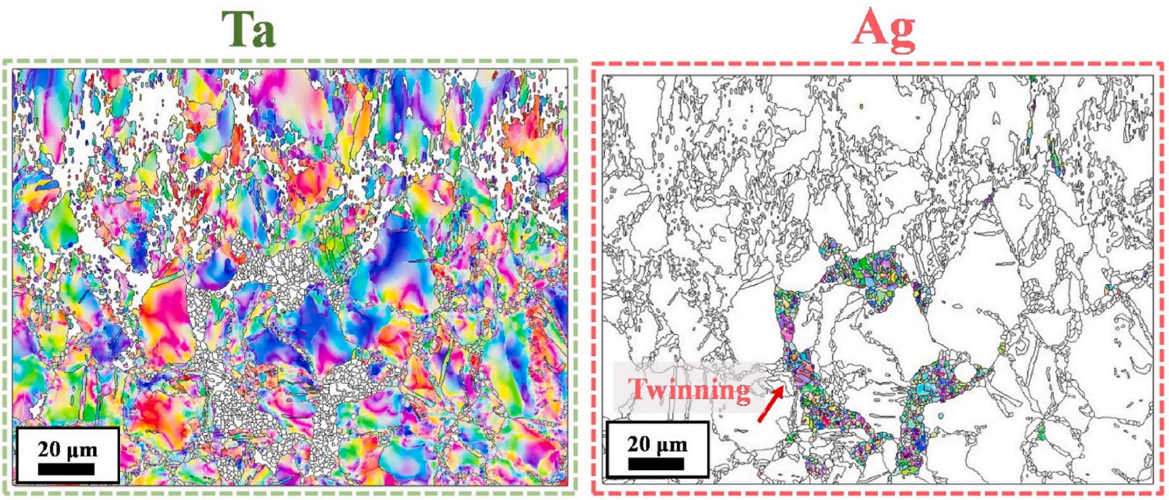

(a) Ta-2Ag

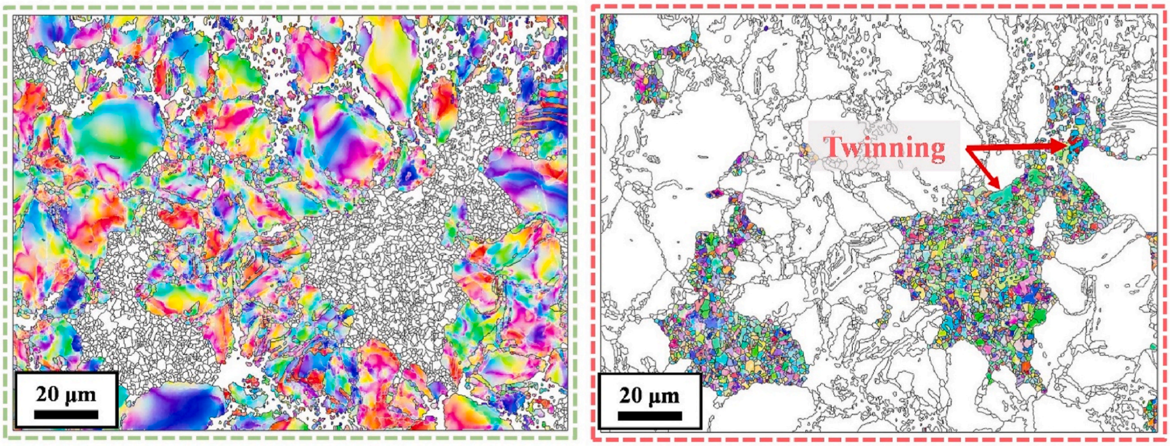

(b) Ta-5Ag

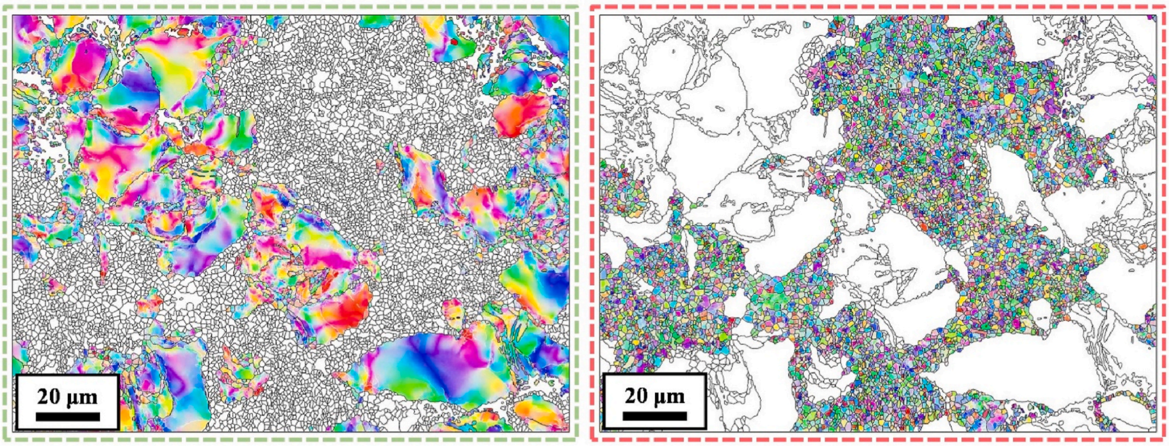

(c) Ta-10Ag

Fig. 3. EBSD IPF mapping of cold sprayed Ta/Ag composites (a) Ta–2Ag, (b) Ta–5Ag and (c) Ta–10Ag coatings.

converging-diverging de-Laval nozzle. Ultimately, powder particles impact the substrate, resulting in severe deformation. Then, deposition is produced via atomic diffusion or mechanical interlocking. Moreover, the high-velocity impact of powder particles in cold spray not only cleans the oxide layer from the Mg substrate surface, simplifying surface preparation, but also creates a compressive layer on the substrate, enhancing the fatigue properties of the Mg substrate [20]. These advantages make CS an ideal method for producing protective coatings on magnesium alloys. For instance, Wei et al. [21] demonstrated an in-situ shot-peening effect during the cold spraying of nickel coatings on AZ31B magnesium alloy. The cold-sprayed (CSed) nickel coating was densified by this enhanced peening effect, resulting in excellent protection for AZ31B magnesium and strong adhesive strength. Similarly, Daroonparvar et al. [22] fabricated a multi-layer Al/Ta/Ti coating using

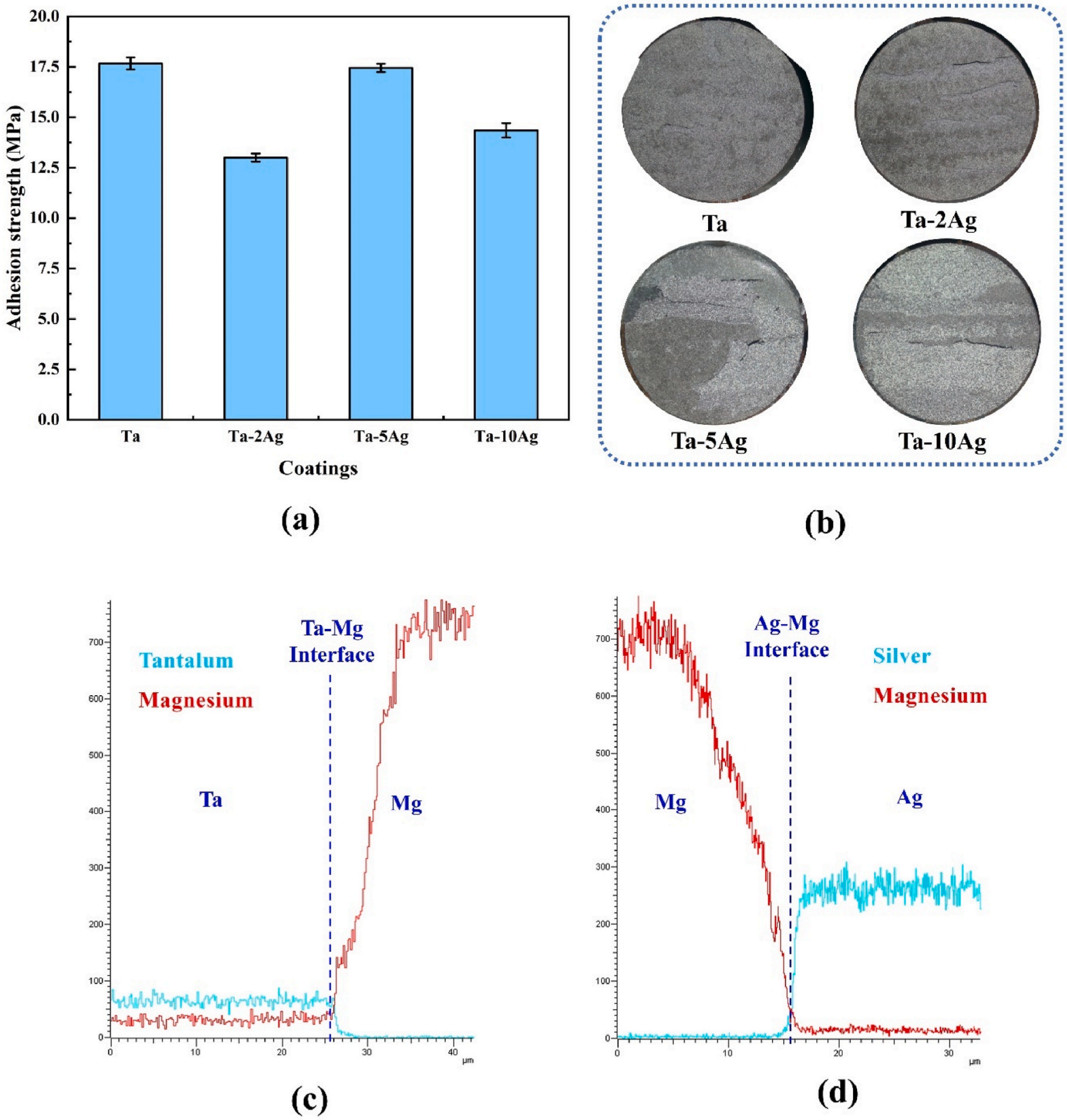

Fig. 4. (a) adhesive strength and (b) fracture surface after pulling-off testing. And EDS line scan of the coating substrate interface, (c) Ta–Mg interface and (d) Mg–Ag interface.

cold spray, which also provided superior protection for the magnesium alloy substrate. These cold-sprayed coatings exhibited reliable corrosion resistance in long-term testing, revealing the promising potential of cold spray technology for producing protective coatings on magnesium alloys.

In addition to producing single-material coatings, cold spray technology can also be used to manufacture metal matrix composites (MMCs) by simply mixing matrix and enhancement material powders [28]. Compared to single-material coatings, MMCs offer tunable properties by selecting specific functional or reinforcement materials [29–31]. This flexibility allows for the induction of specific biofunctions, such as antibacterial properties, which can further enhance the performance of biomedical devices and reduce the side effects experienced by patients [32–34]. Moreover, the different mechanical properties between the matrix and reinforcement materials can induce an in-situ peening effect that densifies the coating, providing additional protection by further isolating substrates from corrosive electrolytes [34,35]. As a result, cold-sprayed MMC coatings are expected to offer more comprehensive protection than coatings made from single materials. However, the physical and chemical differences between the matrix and the composite materials can lead to galvanic corrosion, which may cause significant degradation of the matrix material. Nevertheless, by carefully selecting material combinations, it is possible to shift galvanic corrosion toward cathodic protection, thereby extending the longevity of the composite coatings.

Considering the advantages of cold spray and MMCs, tantalum (Ta), known for its excellent corrosion resistance and biocompatibility, and silver (Ag), recognized for its reliable antibacterial properties, were used to fabricate Ta/Ag MMC coatings on Mg alloy via cold spray [36–38]. To evaluate their protective effects on Mg alloys, a series of tests, including adhesion, corrosion resistance, and wear resistance, were conducted. Based on the results of these tests, the adhesion, corrosion, and wear mechanisms were analyzed, providing valuable insights for further enhancing the long-term protection of Ta/Ag composites on Mg alloy

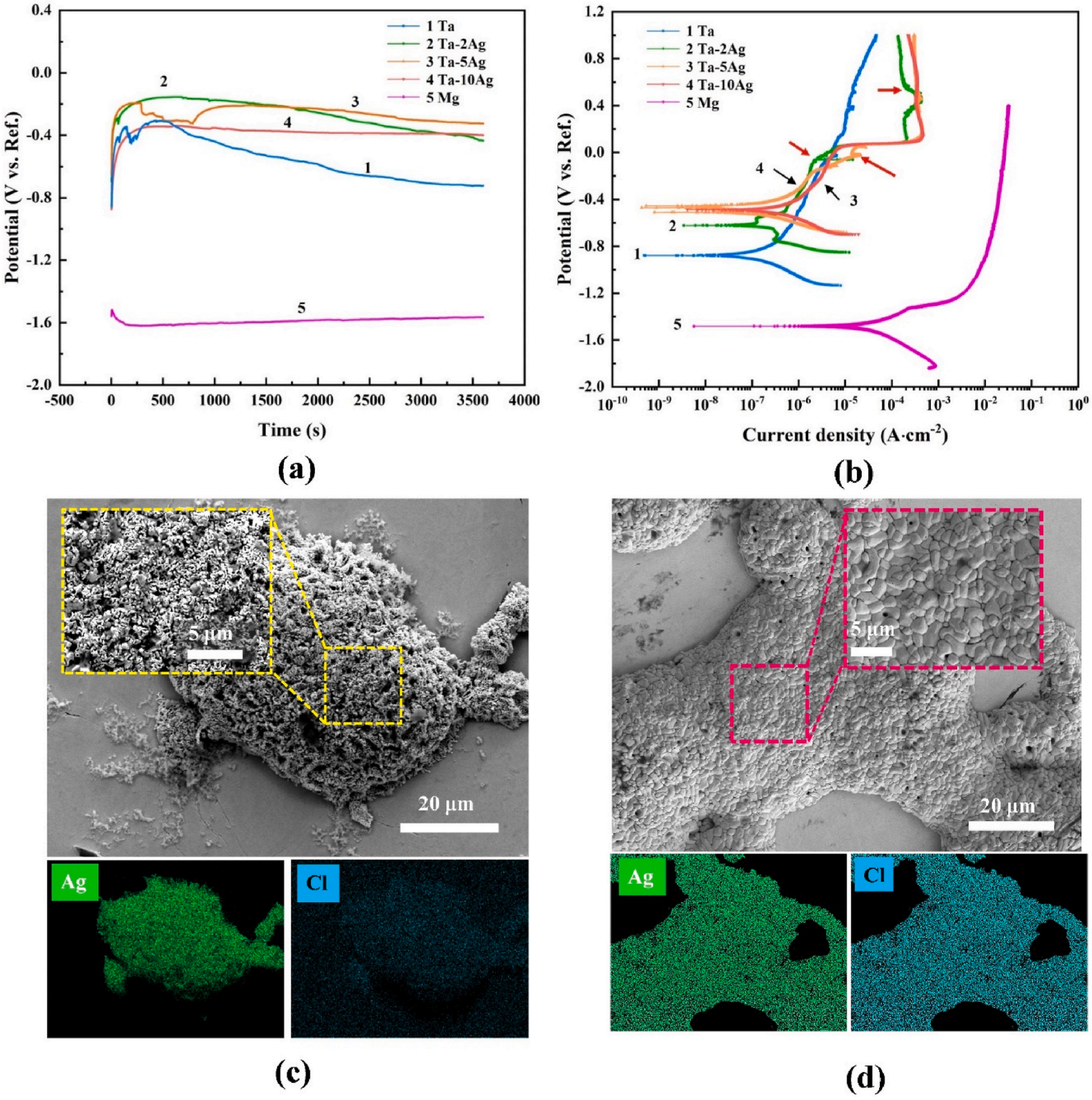

Fig. 5. (a) OCP curves and (b) PDP curves of Ta and Ta/Ag composites coated AZ31B Mg alloy in SBF solution.(c) and (d) microstructure of Ag agglomerations after PDP testing.

implants.

2. Materials and methods

2.1. Substrate preparation and cold spray process

AZ31B magnesium plates, consisting of 97% Mg, 2.56% Al, and 0.8% Zn, were used as the substrate for the experiment. Before applying the cold spray process, the surface of the magnesium plates was sand blasted to remove the oxide layer and then cleaned thoroughly with acetone.

Special-grade tantalum powder (H.C. Starck Inc., Germany) with an average particle size of 29.5 μm, along with gas-atomized silver powder averaging 39.8 μm, were employed in the cold spray process. Before spraying, the silver powder was mechanically blended with tantalum in volume ratios of 2%, 5%, and 10% using a Turbula shaker. These mixtures were designated as Ta–2Ag, Ta–5Ag, and Ta–10Ag, corresponding to their silver content.

During the cold spray process, the pre-mixed powders were directly fed into the main gas stream to form Ta/Ag composite coatings. Due to the significant difference in physical and mechanical properties between Ta and Ag, the window for a successful deposition is narrow. After several trials, the cold spray parameters were optimized as follows: nitrogen (N_2) was used as the carrier gas at a pressure of 30 MPa and a temperature of 600 °C. This condition is able to ensure effective deposition of tantalum while avoid nozzle clogging that could occur due to the softer silver particles.

2.2. Microstructure characterization

The microstructure including the coating microstructure and morphology produced after the cold spray were observed by Zeiss ultra-scanning electronic microscope (SEM) and composition information were analyzed by energy-dispersive X-ray spectroscopy (EDS, Oxford Instrument). A more detailed grain structure was characterized by electron backscatter diffraction (EBSD) using Bruker e-FlashHR EBSD detector. Before performing EBSD testing, all samples underwent grinding and final polishing with colloidal silica. The obtained EBSD data were analyzed using the open-source MTEX code.

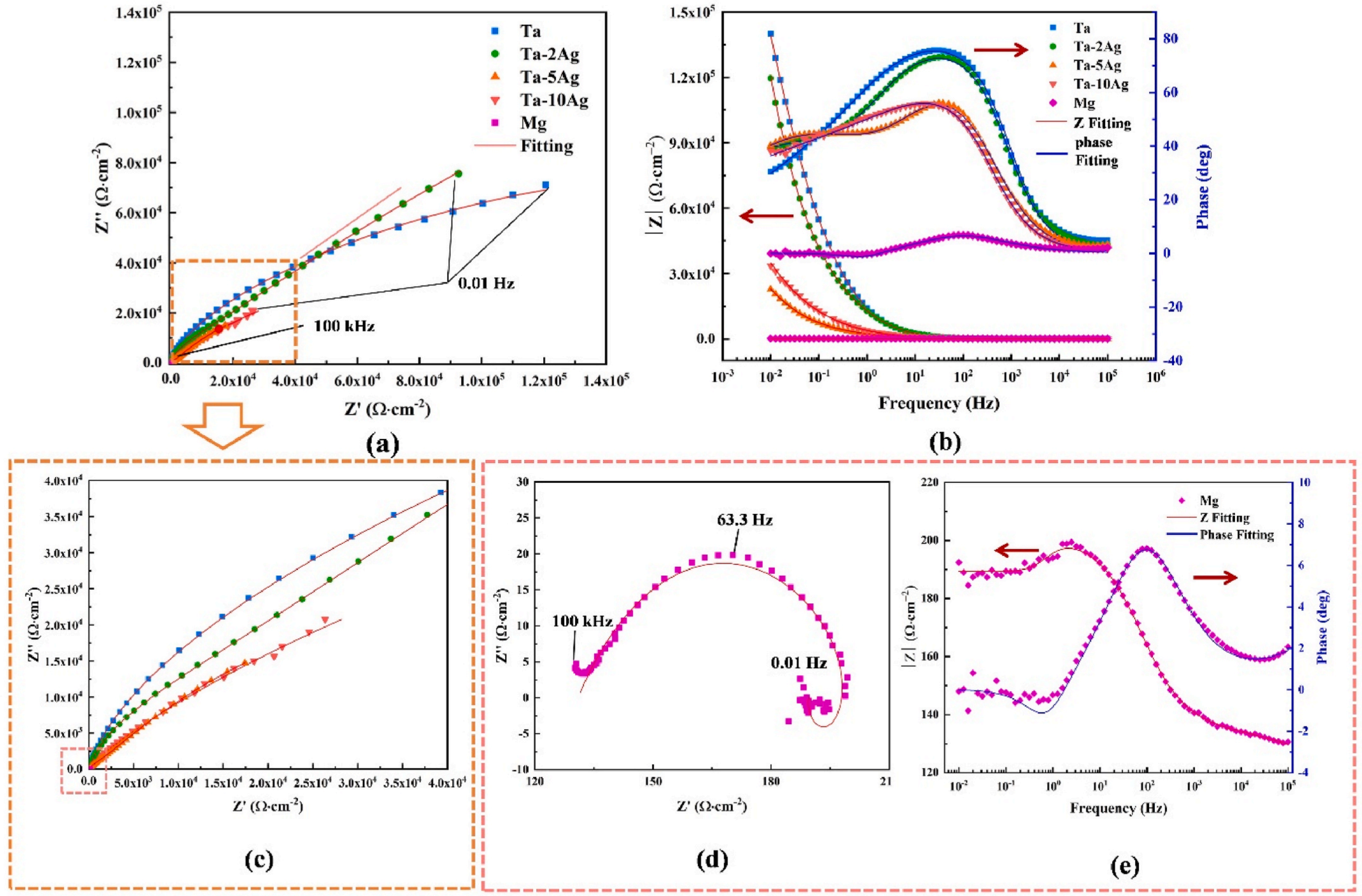

Fig. 6. EIS Nyquist plots and Bode plots. (a) Nyquist plots of bare and coated AZ31 alloy, (b) the Bode plots of bare and coated AZ31 alloy, (c) the enlarged Nyquist plots of bare Mg alloy, (d) the enlarged Bode plots of bare AZ31 Mg alloy.

2.3. *Adhesion strength testing*

After the cold spray process, the adhesive strength between the Ta/Ag coating and the Mg substrate was evaluated using a pulling-off test, in accordance with ASTM D903 standards. A thermal curing adhesive tape with a strength of 80 MPa was used for the adhesive testing. For the testing, a cylindrical Ta/Ag coated Mg sample with a diameter of 2 cm was cut from the Ta/Ag coated Mg plate using electrical discharge machining (EDM). The coating surface, which would be in contact with the adhesive tape, was sandblasted and cleaned with acetone to ensure optimal adhesion. Following the cleaning process, the coated Mg sample was adhered to a counter mould made of stainless steel to create a specimen for adhesive strength testing, as illustrated in Fig. 1b. A tensile strength testing machine was used to pull the adhered sample and the counter apart. The adhesive strength of the coating was then calculated based on the force required for separation. The adhesive strength test was repeated six times for each type of coating, and the adhesive strength was calculated as the average value.

2.4. *Corrosion testing*

To exclude the influence of coating thickness and surface roughness, all coatings were milled to a uniform thickness of approximately 200 μm before corrosion testing. The tested surface was then ground and polished with 0.06 μm colloidal silica. Electrochemical testing was conducted on the Ta/Ag composite-coated AZ31B Mg plates using simulated body fluid (SBF) as the electrolyte, to simulate in-body corrosion conditions. The constituation of SBF is show in Table 1. All samples are round with a diameter of 10 mm. The open circuit potential (OCP), potentiodynamic polarization (PDP), and electrochemical impedance spectroscopy (EIS) tests were conducted sequentially by using a conventional three-electrode setup in a specially designed testing cell for coatings, as illustrated in Fig. 1c, in which only top surface of coating was exposed to the electrolyte. For the testing, an Ag/AgCl electrode was used as the reference electrode and a platinum bar was used as a counter electrode to complete the electrical circuit.

In the PDP testing, the potential scan started from −0.5 V to 1.5 V relative to the OCP. During the EIS testing, a sinusoidal AC perturbation with an amplitude of 10 mV and a frequency range from 100 kHz to 0.01 Hz was applied.

To evaluate the long-term corrosion protection ability of the Ta/Ag coating, the Ta/Ag coated Mg alloys were immersed in the SBF solution for 30 days in corrosion test. EIS measurements were conducted every 7 days during the immersion process to assess the corrosion characteristics of the Ta/Ag coated samples over time.

2.5. *Tribology testing*

Pin-on-disc testing was carried out by using Anton Par TRB3 tribometer to evaluate the wear protection of CSed Ta-xAg composites coatings on AZ31B Mg alloy. The wear track length was set to 200 m, with a track radius of 7 mm. A normal load of 10 N was applied during the test. The arm moved at a speed of 250 rpm, corresponding to a linear speed of 183.52 mm/s. For all tests, a 100Cr6 steel ball with a radius of 3 mm was used as the counter wear body. After testing, the material lost was measured by white light interferometry (WLI) and the wear rate is calculated through the following equation:

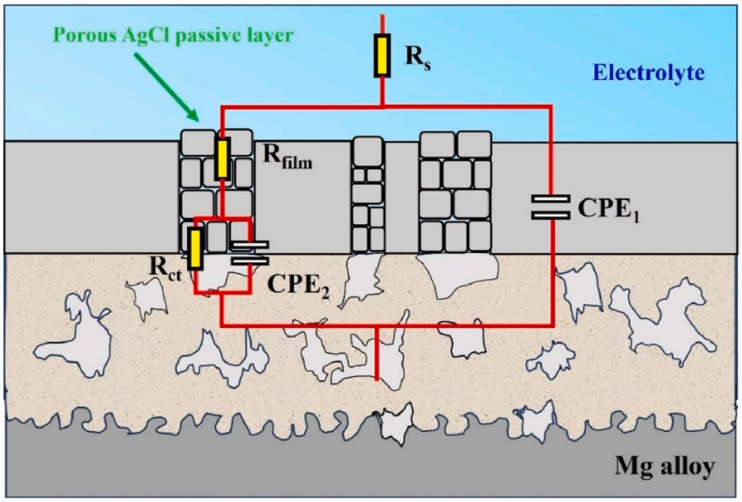

Parameters of EEC elements

	R_s ($\Omega\cdot cm^{-2}$)	R_{film} ($\Omega\cdot cm^{-2}$)	R_{ct} ($\Omega\cdot cm^{-2}$)	CPE1		CPE2	
				Q (Ω^{-1} cm^{-2} s^{-n})	n_e	Q (Ω^{-1} cm^{-2} s^{-n})	n_e
Ta	68.0	$1.096x10^4$	$3.64x10^6$	$1.13x10^{-5}$	0.89	$7.15x10^{-6}$	0.64
Ta-2Ag	72.4	$5.24x10^3$	$1.95x10^5$	$1.11x10^{-5}$	0.89	$1.05x10^{-4}$	0.55
Ta-5Ag	65.9	$1.156x10^3$	$1.28x10^5$	$2.11x10^{-5}$	0.83	$6.75x10^{-5}$	0.54
Ta-10Ag	75.4	$6.94x10^3$	$2.55x10^5$	$2.77x10^{-5}$	0.80	$7.61x10^{-5}$	0.42

Fig. 7. Equivalent electric circuit fitting from the EIS data.

$$W = \frac{V}{F \bullet L}$$

Here, W (mm^3/N·m) is the wear rate, V(mm^3) is the volume of material lost, F (N) is the normal load and L (m) is the slide distance.

3. Results and discussions

3.1. *Microstructure of Ta/Ag composites coatings*

Fig. 2 shows the cross-section (along the thickness direction) SEM images of cold-sprayed Ta/Ag coating on Mg alloy plates. Despite the immiscibility between Mg and Ta, Ta/Ag composite coatings were successfully deposited onto the Mg substrates. Examination reveals that the coatings are dense, with minimal porosity and occasional unbonded interfaces between splats. The low porosity is likely due to the enhanced peening effect, which resulted from decreased deposition efficiency due to the low cold spray parameters and the synergistic behaviour during the cold spraying of pre-mixed Ta/Ag powder. The addition of silver (Ag) increased the porosity and unbonded boundaries (indicated by the yellow arrow in Fig. 2c), particularly near the silver agglomerates. At the Ta–Ag interface, the coating exhibits a zigzag boundary with the Mg substrate, with some Ta particles embedded in the substrate, indicating significant deformation of the Mg surface and mechanical interlocking of the first Ta layer. Notably, the Ag volume in the pre-mixed Ta/Ag powder has minimal effect on the profile of the zigzag boundary, suggesting it does not significantly impact the bonding of the Ta/Ag composite coatings.

Fig. 3 presents the inverse pole figure (IPF) mapping obtained via EBSD. The tantalum (Ta) splats maintain their original angular shape, surrounded by a layer of refined grains formed by dynamic recrystallization (DRX) due to severe deformation at the impact interface. In contrast, the silver (Ag) matrix shows no distinct splat boundaries, suggesting more extensive deformation of Ag during the cold spray process. Refined Ag grains fully cover the Ag agglomerates, indicating a more complete DRX process.

Notably, in the Ta–2Ag and Ta–5Ag coatings, the grains are larger, and twinning is observed, particularly in grains significantly larger than the surrounding ones, indicating annealing twinning. The variation in Ag grain structure across the Ta/Ag composite coatings results from different thermomechanical histories, which are influenced by the volume of soft Ag in the powder and the synergistic deposition behavior during the cold spray process [39].

3.2. *Adhesives strength*

As shown in Fig. 4a, the adhesive strength of the Ta/Ag composite coatings on AZ31 Mg alloys, measured via pull-off tests, ranged from 22.56 MPa to 27.5 MPa. These values are comparable to those of nickel coatings produced by electroless deposition [40,41]. Fracture surface observed by optical microscopy (Fig. 4b) reveals that failure occurred within the coating rather than at the interface with the substrate. The fracture surface of the Ta–10Ag coating exhibits silver agglomerations with a distinct shiny, white appearance (highlighted by red arrows), suggesting that failure likely originated at unbonded boundaries, particularly at the Ta–Ag interface. Consequently, the measured adhesive strength is more consistent than if failure had occurred at the coating-substrate interface, and the actual adhesive strength is likely higher than the recorded values. These findings indicate that the coatings are suitable for biomedical applications, where high load-bearing conditions are not typically required.

To investigate the bonding mechanism, EDS line scans were

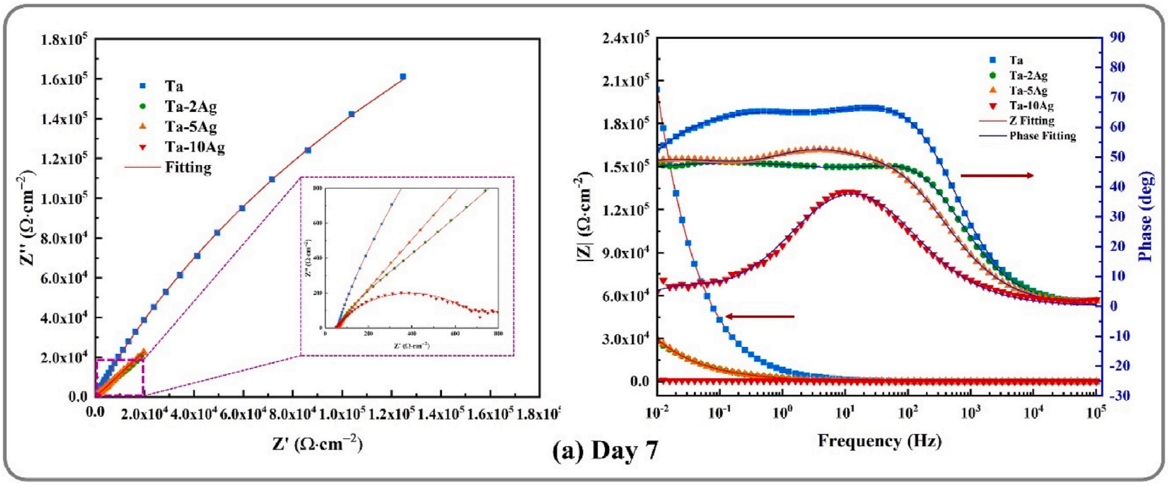

(a) Day 7

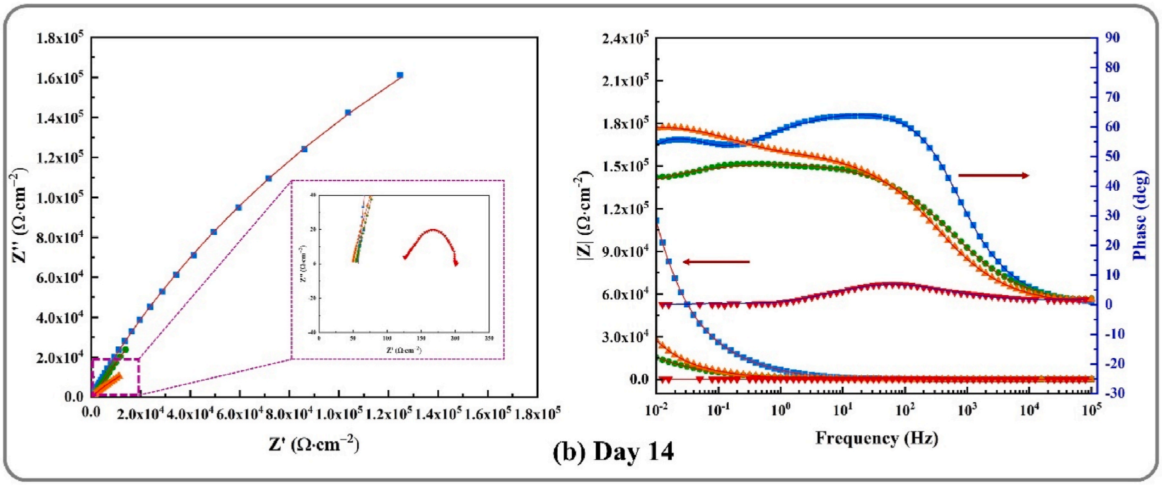

(b) Day 14

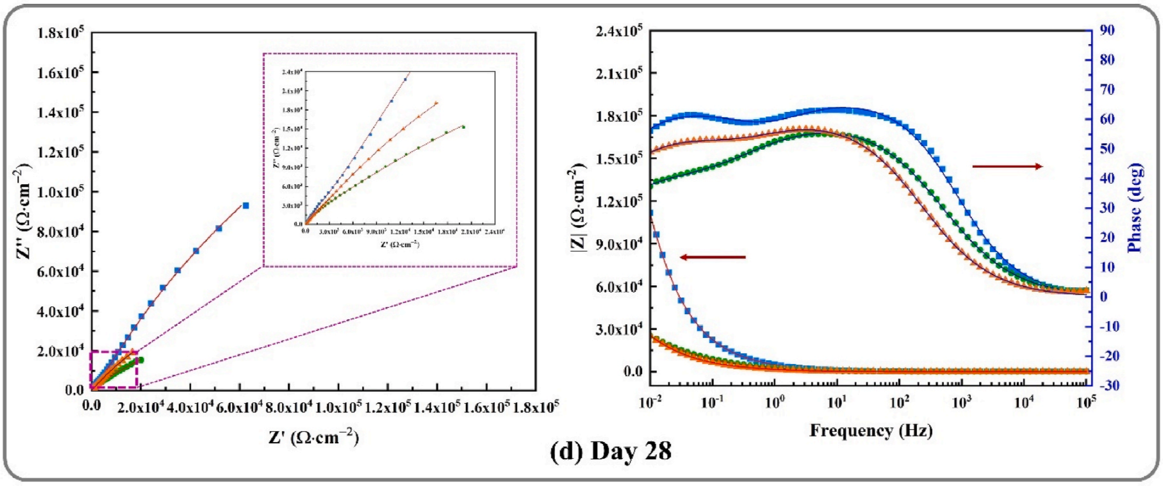

(d) Day 28

Fig. 8. EIS Nyquist and Bode plot measured after (a) 7 days, (b) 14 days and (d) 28 days of immersion in SBF.

performed at the Ta–Mg and Ag–Mg interfaces, as indicated by the red lines in Fig. 2c and d. At the Ta–Mg interface (Fig. 4c), the X-ray intensity exhibits a sharp transition, indicating the absence of atomic diffusion. In contrast, the Ag–Mg interface (Fig. 4d) shows a gradual change in signal intensity. However, this variation is too subtle to conclusively confirm atomic diffusion at the Ag–Mg interface. Even if atomic diffusion occurs between Ag and Mg, the limited volume of Ag is insufficient to significantly affect the final adhesive strength. Therefore, the primary bonding mechanism between the Ta/Ag coatings and the Mg alloy substrate is mechanical interlocking, primarily driven by Ta and Mg.

3.3. *Corrosion resistance*

3.3.1. *Open circuit potential*

Fig. 5a shows the OCP curves of coated and uncoated AZ31B Mg alloys. The coated AZ31B exhibits a more positive potential than the uncoated counterpart, with the OCP becoming increasingly positive as the noble Ag content in the coating increases. The uncoated AZ31B maintains a nearly constant OCP of approximately −1.6 V, indicating

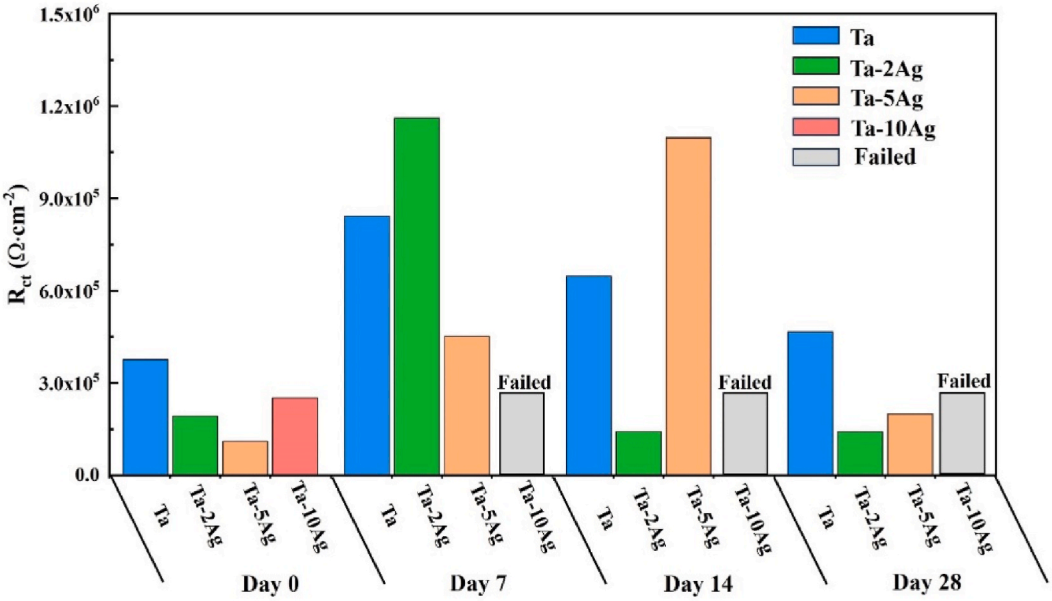

Fig. 9. R_{ct} values in EEC after different periods of immersion.

stable ion exchange at the Mg alloy surface.

In contrast, the OCP of Ta and Ta/Ag composite-coated samples rapidly shifts to a more positive potential, attributed to the noble potential of Ta and Ag and the formation of a passivation layer on the coating surface. As testing goes on, the OCP of the coated samples gradually becomes more positive initially, then slowly decreases, and finally stabilizes at a more negative value. This behavior suggests that the coatings provide good protection at the start of testing, but the protection is gradually compromised, with a subsequent rebuild of protection once the OCP reaches a more negative value. Notably, as the Ag content increases, there is less reduction in the OCP, indicating that higher Ag content improves corrosion resistance.

3.3.2. *Potentiodynamic polarization*

The PDP testing results provide detailed insights into the passivation behavior of Ta/Ag coatings on AZ31B Mg alloy. As shown in Fig. 5b, the Ta/Ag-coated AZ31B alloys exhibit a significant decrease in corrosion current compared to the uncoated AZ31B, with the pure Ta coating not showing a clear passivation stage as the applied potential increases.

In contrast, the Ta/Ag composite-coated samples display a stable passivation stage at an applied potential of around 0.0 V vs Ref. Notably, the PDP curves of Ta–2Ag and Ta–5Ag show oscillations (indicated by red arrows), suggesting an unstable passivation layer. The Ta–10Ag coating, however, exhibits a smooth PDP curve with a stable passivation stage. Fig. 5c and d show the surface microstructure of Ta–5Ag and Ta–10Ag after PDP testing. A porous AgCl layer forms on the Ag agglomerations, while the Ta matrix remains smooth and free of corrosion marks. The AgCl layers differ in characteristics: the Ta–5Ag layer is highly porous, while the Ta–10Ag layer is denser.

These observations suggest that corrosion primarily occurs on the Ag agglomerations within the Ta/Ag composites. The unstable passivation behaviour observed in Ta–5Ag during PDP testing is attributed to the production of the high porosity of the AgCl layer. The formation of AgCl in Ta/Ag composites has been previously discussed in Ref. [39]. The varying porosity of the AgCl layer is influenced by the microstructure of the Ag agglomerations, particularly dislocation density and grain size, which govern the rate of Ag dissolution. In Ta–5Ag, the lower dislocation density results in slower dissolution, leading to a more porous AgCl layer. In contrast, the higher dislocation density in Ta–10Ag accelerates Ag dissolution, resulting in a denser, thicker AgCl layer.

3.3.3. *Electrochemical impedance spectroscopy*

Fig. 6 shows the EIS results for uncoated and coated AZ31B Mg alloys. In the Nyquist plot (Fig. 6a), the uncoated AZ31 displays a small capacitive loop and a low-frequency inductive loop, characteristic of Mg alloys with poor corrosion resistance. In contrast, Ta/Ag MMC-coated samples exhibit larger capacitive loops, indicating enhanced corrosion protection for the Mg substrate. Among the coatings, the pure Ta coating has the largest capacitive loop, reflecting the best corrosion resistance. The Ta–2Ag coating shows a smaller capacitive loop than pure Ta but larger than those of Ta–5Ag and Ta–10Ag, suggesting better corrosion resistance than Ta–5Ag and Ta–10Ag. Zooming into the dashed-line square in Fig. 6a, the capacitive loop of Ta–10Ag is larger than that of Ta–5Ag, indicating that Ta–10Ag offers better corrosion resistance than Ta–5Ag (Fig. 6c).

Based on the EIS results, an equivalent circuit (EEC) was constructed to fit the data. The Nyquist plot of the Ta/Ag-coated Mg samples shows imperfect circular capacitive loops, indicating that a constant phase element (CPE) should be used instead of an ideal capacitor. Additionally, the Bode phase plot reveals a flattened and broad peak in the intermediate frequency region, resulting from the absorption of multiple capacitive peaks. This is particularly evident in the Ta–5Ag-coated Mg, where two distinct peaks are observed.

Thus, it is inferred that two CPE elements should be included in the EEC. The constructed EEC, shown in Fig. 7, is a typical model for analyzing the dynamic electrochemical behavior of coating systems [42]. The fitting results, represented by the red line in the Nyquist and Bode plots, closely match the experimental data, confirming the validity of the constructed EEC. The parameters of the EEC elements are listed in the Table of Fig. 7.

In the equivalent electrical circuit, the resistance of the electrolyte (Rs) is located between 65 Ω and 75 Ω. R_{film} is the resistance of the passivation layer on the coating surface. Fitting results indicate that the pure Ta coating exhibits the highest R_{film} attributed to its dense and stable Ta_2O_5passive layer. The addition of Ag significantly reduces R_{film}. As Ag content increases from 2 vol% to 5 vol%, R_{film} decreases but rises again at 10 vol% Ag. This variation is due to the characteristics of the AgCl passive layer. The porous AgCl layer on Ag agglomerates lowers R_{film} with its density dictating this behavior. The Ta–10Ag coating, featuring the densest AgCl layer (Fig. 5d), achieves a higher R_{film} compared to Ta–2Ag and Ta–5Ag coatings.

The charge transfer resistance (R_{ct}) exhibits a similar trend. The pure

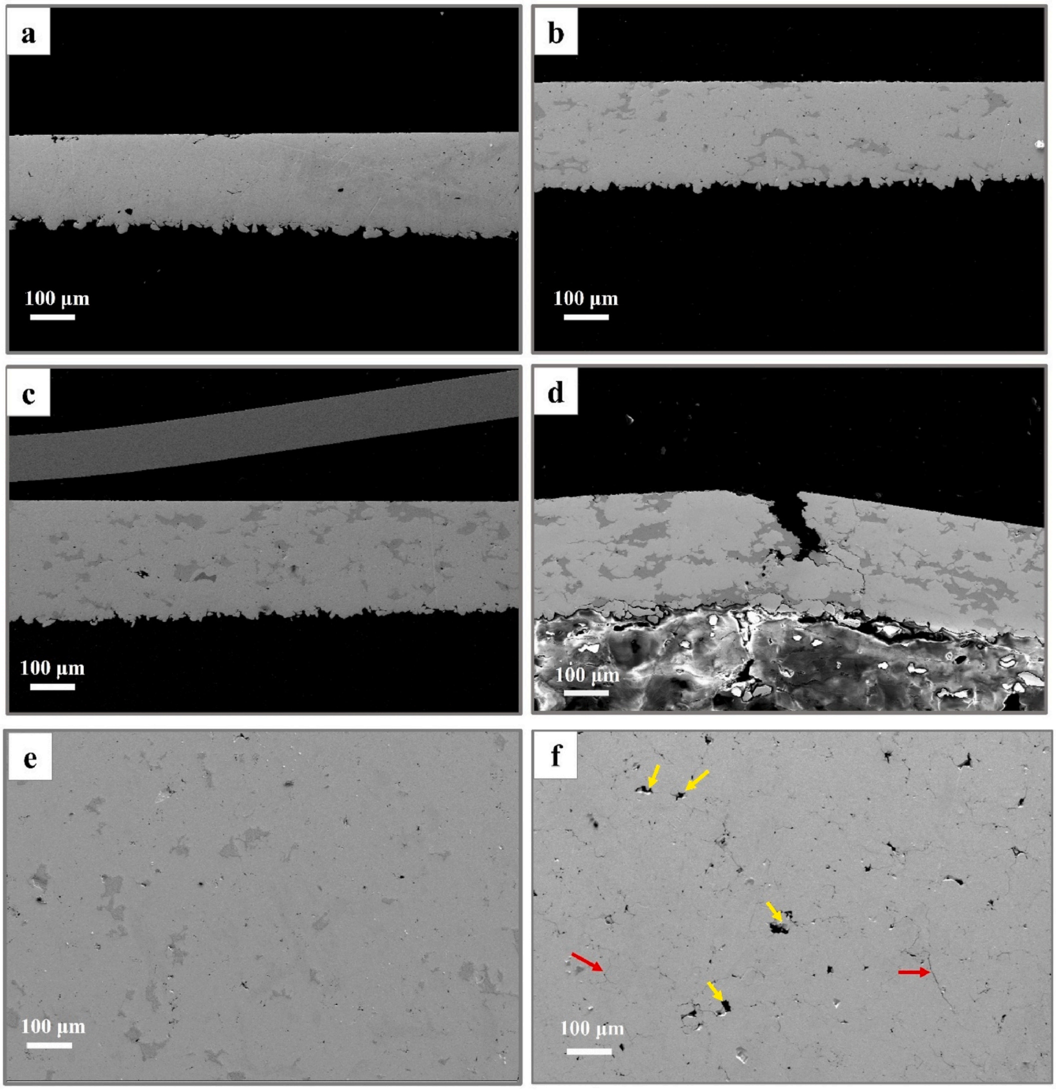

Fig. 10. Cross-section and the top surface of coated AZ31B Mg alloys after 28 days of immersion (a) pure Ta coating, (b) Ta–2Ag coating, (c) Ta–5Ag coating, (d) Ta–10Ag coating. (e) the top surface of Ta–5Ag and (f) top surface of pure Ta.

Ta coating shows the highest R_{ct}, reflecting its superior corrosion resistance. However, R_{ct} decreases with the addition of Ag due to insufficient passivation by the AgCl layer. Among Ta/Ag coatings, Ta–10Ag has the highest R_{ct}, indicating the best corrosion resistance. In contrast, Ta–2Ag and Ta–5Ag have lower R_{ct} values, suggesting reduced corrosion resistance. The porosity of the AgCl layer significantly influences corrosion behavior. The dense AgCl layer in Ta–10Ag restricts electrolyte penetration, enhancing corrosion resistance. In contrast, the more porous AgCl layers in Ta–5Ag and Ta–2Ag facilitate Ag agglomerate dissolution. However, the increased Ag dissolution may enhance cathodic protection for the Ta matrix, potentially shielding it from corrosion. Therefore, to assess the real corrosion resistance, an extended-duration immersion test was conducted.

3.3.4. *Extended-duration corrosion testing*

In the immersion test, the non-destructive EIS test was used to monitor the corrosion status. EIS Nyquist and Bode curves were recorded after 7, 14, and 28 days (Fig. 8). The charge transfer resistance (R_{ct}) values for the coated AZ31 Mg alloys, derived from EIS curve fitting, are shown in Fig. 9.

In the Nyquist plots (Fig. 8), the capacitive loop diameter decreases over time, indicating a reduction in corrosion resistance. After 28 days, the pure Ta coating exhibited the largest loop, demonstrating superior corrosion resistance compared to Ta/Ag composite coatings. However, as shown in the inset of Fig. 8b, the Ta–10Ag coating displayed a typical Mg AZ31 EIS curve after just 7 days, indicating coating failure.

Fig. 9 reveals that R_{ct} increased for the Ta, Ta–2Ag, and Ta–5Ag coatings during the first 14 days, suggesting an initial enhancement of their passivation layers. Among these, Ta–2Ag exhibited the most significant increase in R_{ct}, outperforming both Ta and Ta–5Ag. Beyond 14 days, the R_{ct} values for Ta and Ta–2Ag began to decline, indicating degradation of the Ta_2O_5 passive layer on pure Ta and the dissolution of the AgCl layer on the Ag surface. Conversely, the R_{ct} of Ta–5Ag increased significantly during this period. After 30 days, the R_{ct} values for all coatings returned to levels close to their initial values, signifying further degradation of their passivation layers.

The pure Ta coating maintained consistent R_{ct} values throughout the 28-day immersion, highlighting its stability. In contrast, the R_{ct} of Ta–2Ag and Ta–5Ag showed sharp increases followed by steep declines during the immersion period.

The dense and stable Ta_2O_5 passive layer accounts for the corrosion resistance of the pure Ta coating. For Ta/Ag composites, the R_{ct} decline is attributed to the degradation of the AgCl layer, likely caused by its slow dissolution or the formation of soluble $AgCl_x^{(x-1)-}$ complexes [43].

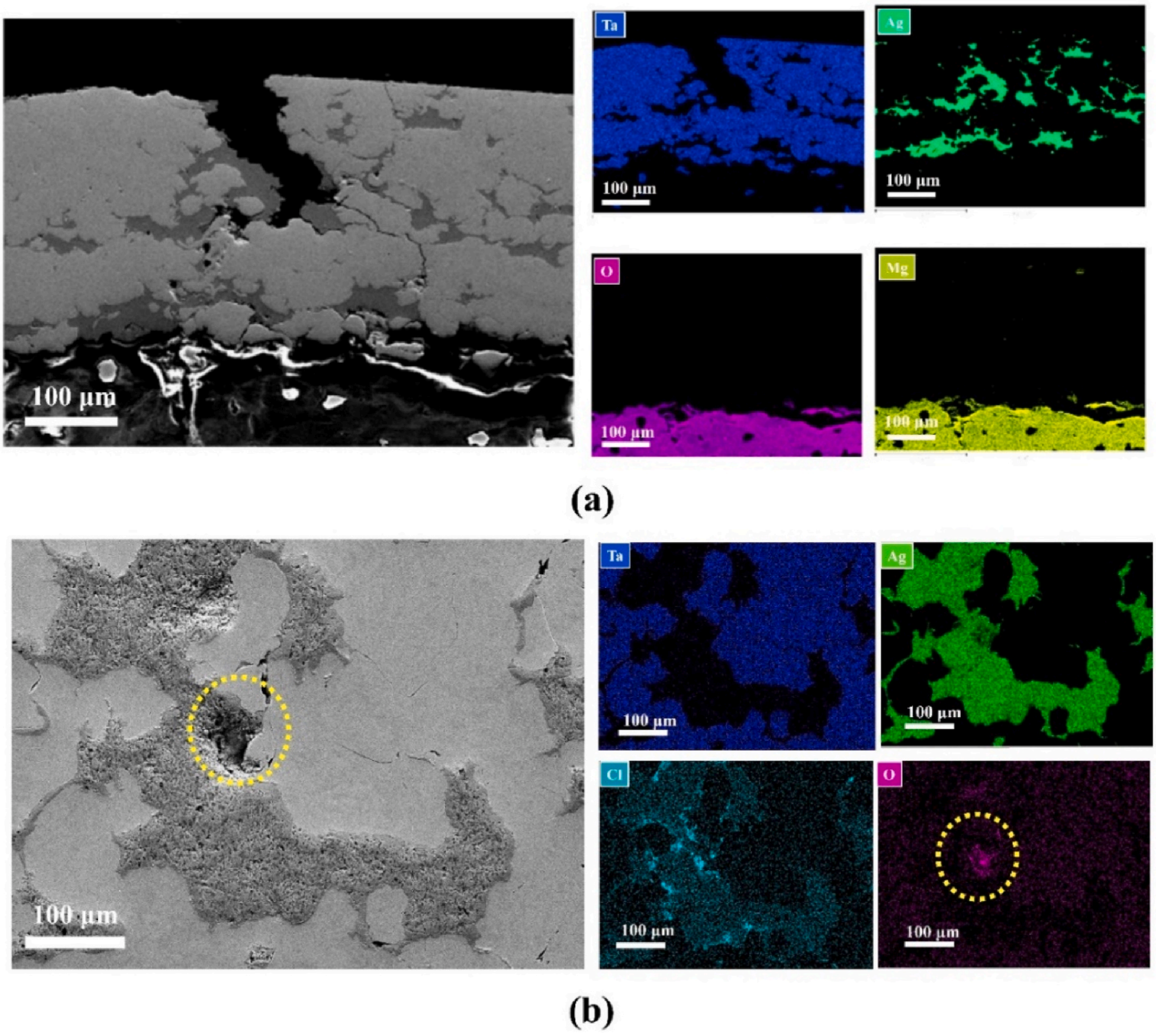

Fig. 11. (a) Zoomed-in cross-section of Ta–10Ag coating and EDS mapping. (b) top surface morphology of Ta–10Ag after 28 days of immersion.

As the AgCl layer dissolves, fresh Ag surfaces are exposed to the electrolyte, reducing R_{ct} values and ultimately returning them to near-initial levels.

To investigate long-term corrosion behavior, the microstructures of tested samples were analyzed. Fig. 10a–d shows the cross-sections of the Ta/Ag coatings. For Ta, Ta–2Ag, and Ta–5Ag coatings, no significant evidence of corrosion was observed from the coating surface to the substrate. However, in the Ta–10Ag coating (Fig. 10d), a cavity with a strong charging effect was found at the interface between the coating and the AZ31B Mg alloy substrate, connected to the coating surface by a channel.

Surface analysis (Fig. 10e and f) revealed a dense and smooth Ta matrix in Ta–2Ag after immersion, while pores and gaps (marked by yellow and red arrows) formed due to Ag dissolution. This indicates that Ag's poor passivation prevents the Ta matrix from corroding, enhancing its corrosion resistance. EDS mapping of the cavity and channel regions (Fig. 11a) detected oxide signals, confirming that the channel serves as a corrosion pathway from the coating surface to the substrate. This pathway originates from an Ag agglomeration on the surface and extends to the substrate interface, with Ag agglomerations beneath the surface interconnected by the corrosion path.

Fig. 11b shows the top surface of the failed Ta–10Ag coating after prolonged immersion. The Ta matrix appears smooth and clean with no significant oxide signals, whereas the Ag surface is rough, with Cl signals indicating localized corrosion. Clear holes (yellow dashed circles) at the Ag–Ta interface suggest this is the primary site of severe corrosion. The edges of Ag agglomerations in Ta–10Ag (Fig. 3) are characterized by fine DDRX grains. The passive AgCl layer in this region is porous, partially preventing Ag dissolution. The close contact between Ag and Ta accelerates galvanic corrosion at these edges due to the short ion migration distance. Additionally, the lack of metallurgical bonding between Ta and Ag increases the unbonded boundary as Ag content rises, allowing electrolytes to penetrate the interface easily and further accelerating corrosion.

The corrosion mechanism of the Ta/Ag coating is schematically illustrated in Fig. 12. Initially, galvanic corrosion occurs between Ag and Ta due to Ta's less negative potential, leading to significant Ta dissolution (Fig. 12I). However, Ta ions readily react with oxygen to form a dense and stable passive layer that halts further corrosion of the Ta matrix. In contrast, Ag agglomerations, being noble and lacking effective passivation, act as anodes in the galvanic cell (Fig. 12II).

During corrosion, severe damage occurs at the Ta–Ag interface on the surface of the Ta/Ag composite coatings. As corrosion progresses, the unbonded Ta–Ag interfaces facilitate the penetration of electrolytes deeper into the coating, acting as shortcuts for corrosion. When the electrolyte encounters another Ag agglomeration deeper within the coating, the corrosion process accelerates. This "frog leap" advancement through unbonded Ta/Ag interfaces eventually reaches the active Mg alloy substrate (Fig. 12III). At this stage, severe corrosion occurs, producing porous MgO and releasing hydrogen gas.

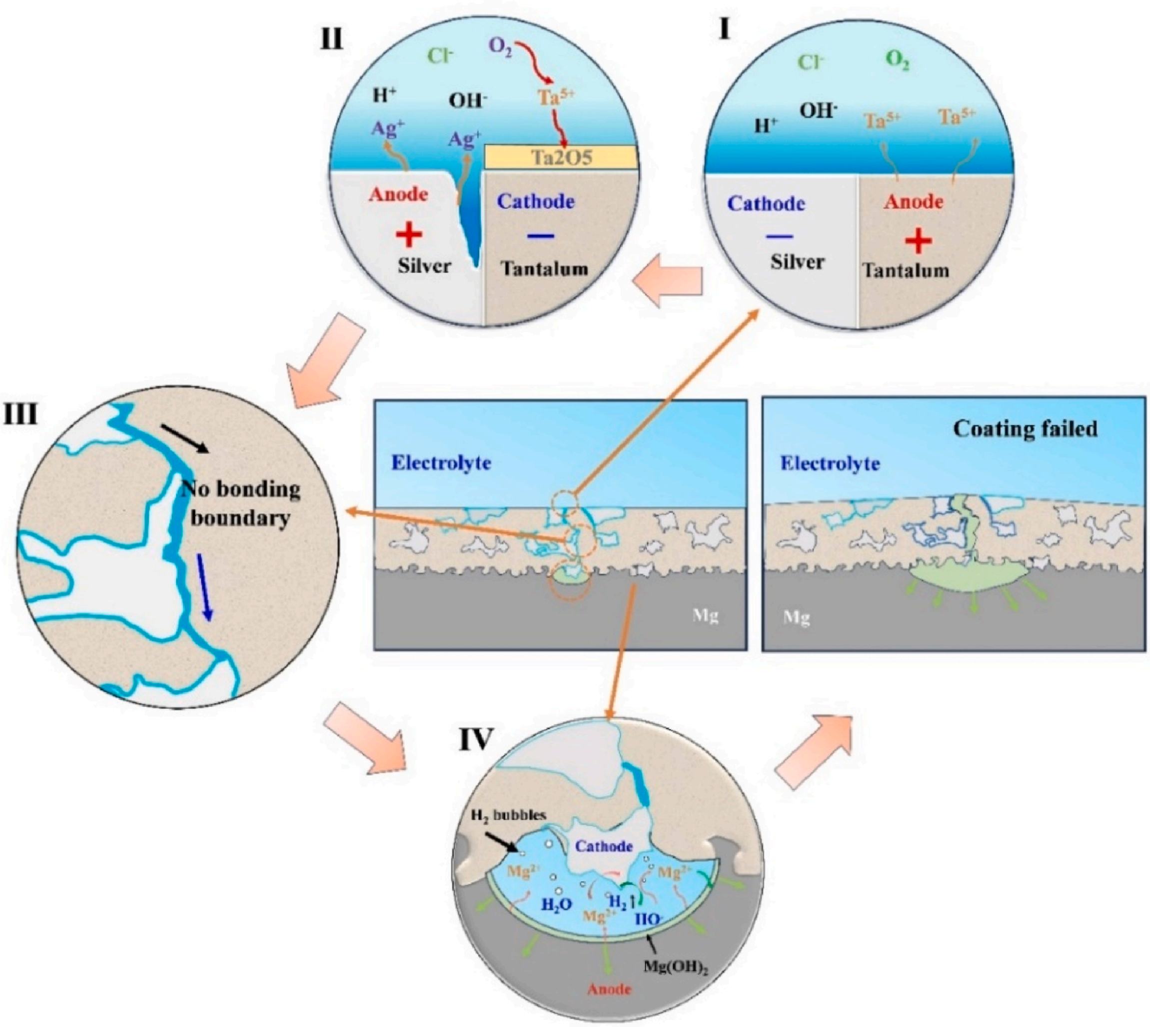

Fig. 12. Schematic corrosion failure mechanism of Ta-xAg composite coating. (I) the dissolution of Ta at the start of corrosion. (II) passive Ta2O5 layer formed on the Ta surface and Ag was dissolved acting as an anode in galvanic corrosion. (III) penetration of the electrolyte via a "frog leap" manner. (IV) electrolyte reaches the Mg substrate, resulting in corrosion of the substrate.

Among the coatings, the Ag agglomerations in Ta–2Ag and Ta–5Ag are less densely distributed and smaller in size compared to those in Ta–10Ag. The greater distance between Ag agglomerations in Ta–2Ag and Ta–5Ag makes it more difficult for the electrolyte to penetrate via the "frog leap" mechanism. Consequently, Ta–2Ag and Ta–5Ag exhibit better long-term corrosion resistance than Ta–10Ag.

3.4. Wear resistance

3.4.1. Morphology of wear tracks

Wear resistance varied among the coatings, as shown in Fig. 14f. Ta–2Ag exhibited the lowest resistance, while Ta, Ta–5Ag, and Ta–10Ag showed similar resistance. The dominant wear mechanism shifted with increasing Ag content: fatigue and abrasive wear prevailed in Ta and Ta–2Ag, while abrasive wear became dominant as Ag content increased. The addition of Ag significantly improved the fatigue wear resistance of cold-sprayed Ta/Ag composite coatings and reduced free debris formation.

After the pin-on-disc wear test, the wear track morphology was investigated using SEM and EDS (Fig. 14), and 3D profiles were obtained with a white light interferometer (WLI) (Fig. 14). SEM-EDS analysis (Fig. 13) revealed an intense oxygen signal in all coatings, indicating oxidation during wear. Ag smearing along the wear track was observed, with higher Ag content promoting a more homogeneous distribution. In pure Ta coatings, Fe signals in flake-like structures suggest material transfer from the steel ball, indicative of adhesive wear. Oxidation is attributed to friction-induced temperature rise, which decreases with increasing Ag content due to its high thermal conductivity.

Debris analysis showed extensive particles and wide, deep grooves on pure Ta and Ta–2Ag tracks (Fig. 13a and b). With 5 vol% Ag, debris reduced but grooves increased (Fig. 13c), while at 10 vol% Ag, the wear track became smooth with narrow grooves and minimal debris (Fig. 13cii). Deep craters on the wear tracks of Ta, Ta–2Ag, and Ta–5Ag coatings suggest significant material removal, with both crater size and number decreasing as Ag content increased. The Ta–10Ag coating exhibited rare large craters, replaced by small pits (Fig,13diii).

Crack networks observed in pure Ta flake structures (Fig,13aiii), and subsequently in Ta–2Ag, and Ta–5Ag coatings, indicate fatigue wear caused by cyclic loading, deformation, and strain hardening. With fatigue fractures propagating cracks, materials were removed from deeper layers beneath the interface. However, in Ta–10Ag, no crack network was observed and a network of Ag was revealed in Fig. 13dii, inducting the Ag filled the crack during the wear.

Wear track profiles (Fig. 14a and b) showed wider and more irregular tracks for Ta and Ta–2Ag, indicating severe material removal and lower fatigue resistance. In contrast, the smoother, V-shaped profiles of Ta–5Ag and Ta–10Ag indicate improved wear resistance, though localized craters persist in Ta–5Ag (Fig. 14c). At 10 vol% Ag, the wear track

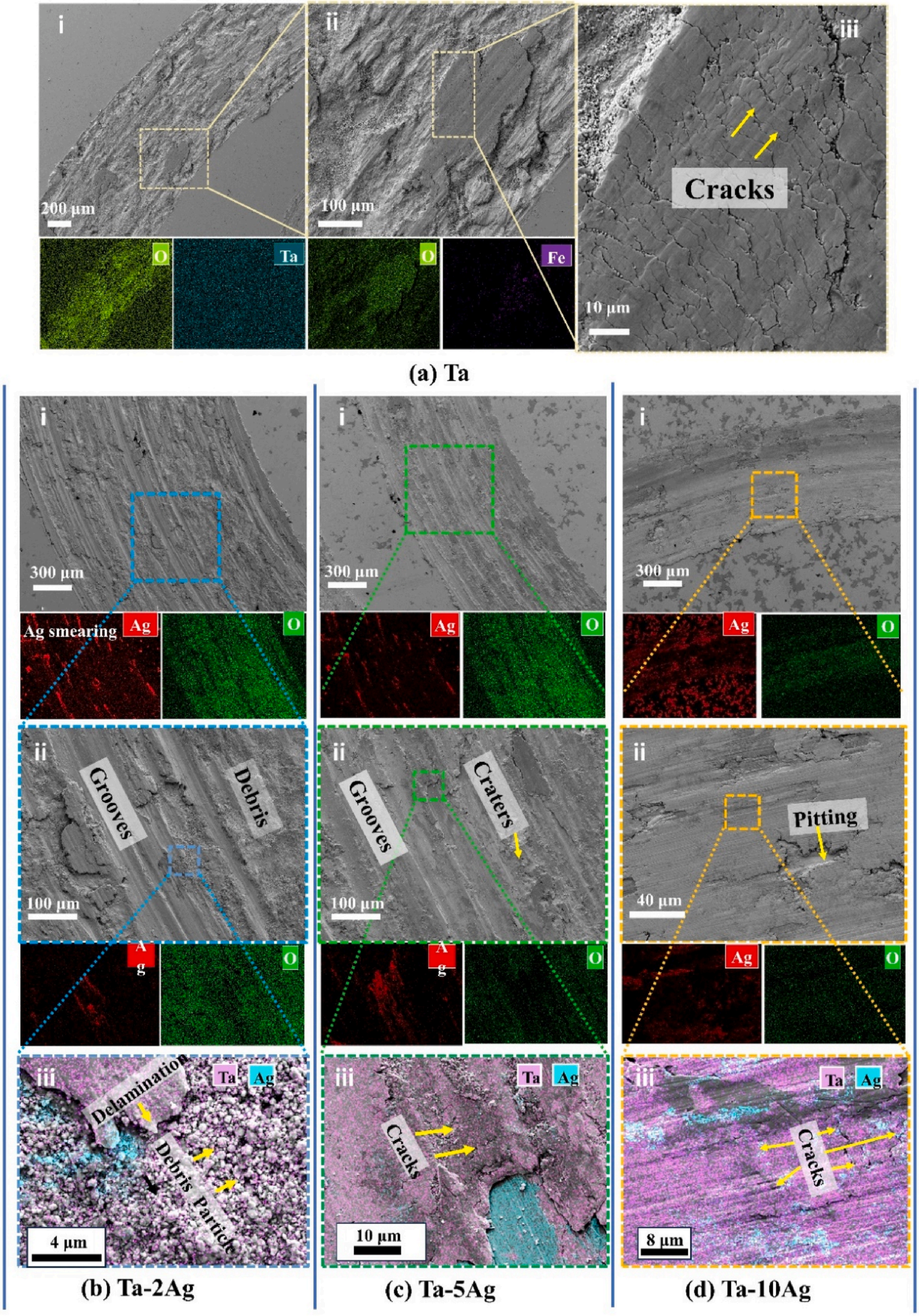

Fig. 13. Morphology of worn surface of (a) pure Ta, (b) Ta–2Ag, (c) Ta–5Ag and (d) Ta–10Ag coatings.

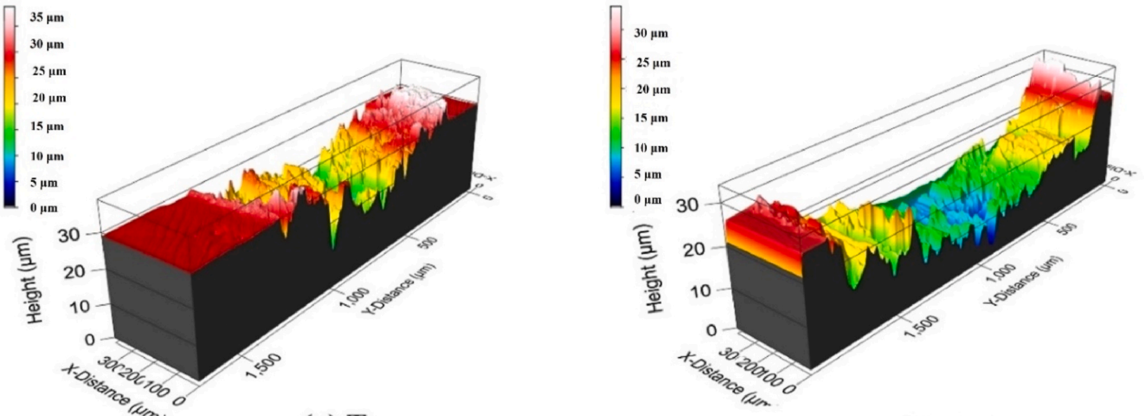

(a) Ta

(b) Ta-2Ag

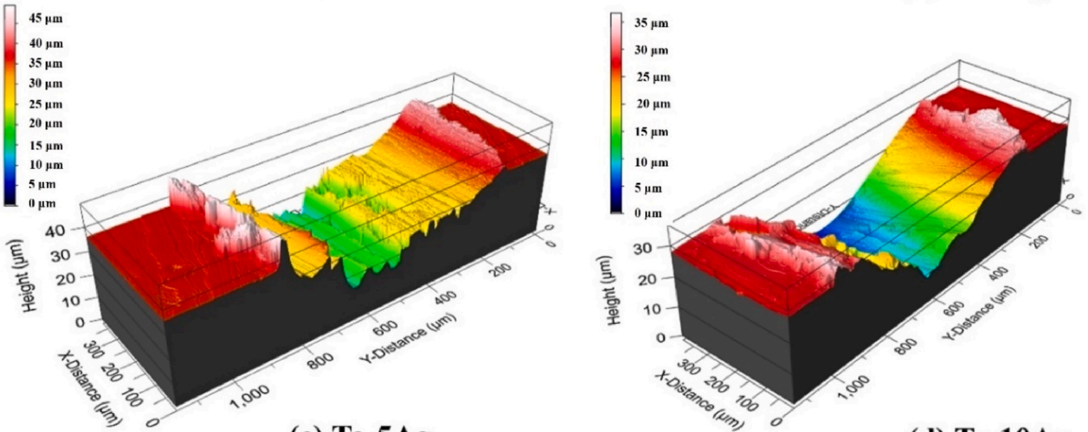

(c) Ta-5Ag

(d) Ta-10Ag

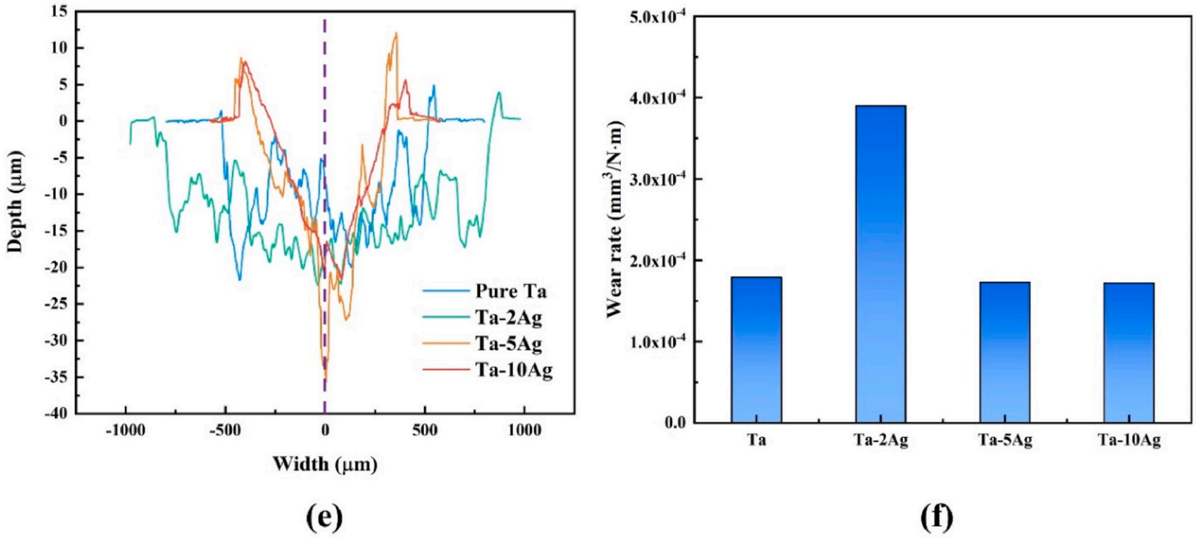

Fig. 14. (a)–(d) 3D profile of wear worn slice mapping WLI.(e) cross section of wear track. (f) wear rate.

becomes smoother and more regular, reflecting enhanced fatigue wear resistance (Fig. 14d). Compared to abrasive and adhesive wear, fatigue wear is more aggressive due to deeper material loss. Moreover, fatigue-induced material removal introduces third-body abrasive particles, which intensify abrasive wear and broaden wear tracks. Cyclic deformation breaks removed material into smaller debris, explaining the widest tracks and abundant debris in Ta and Ta–2Ag coatings. It seems that Ag agglomerates in high Ag contents coating, could fill the crack during the wear, prohibiting crack propagating and minimize fatigue wear.

3.4.2. *Wear mechanism of Ta/Ag composite coating*

The wear behavior and mechanisms of materials are primarily influenced by mechanical properties, surface roughness, and lubrication conditions. In this study, tribology testing was performed without lubrication, and measured surface roughness (in supplementary document) variation was insignificant, highlighting the critical role of the coatings' mechanical properties.

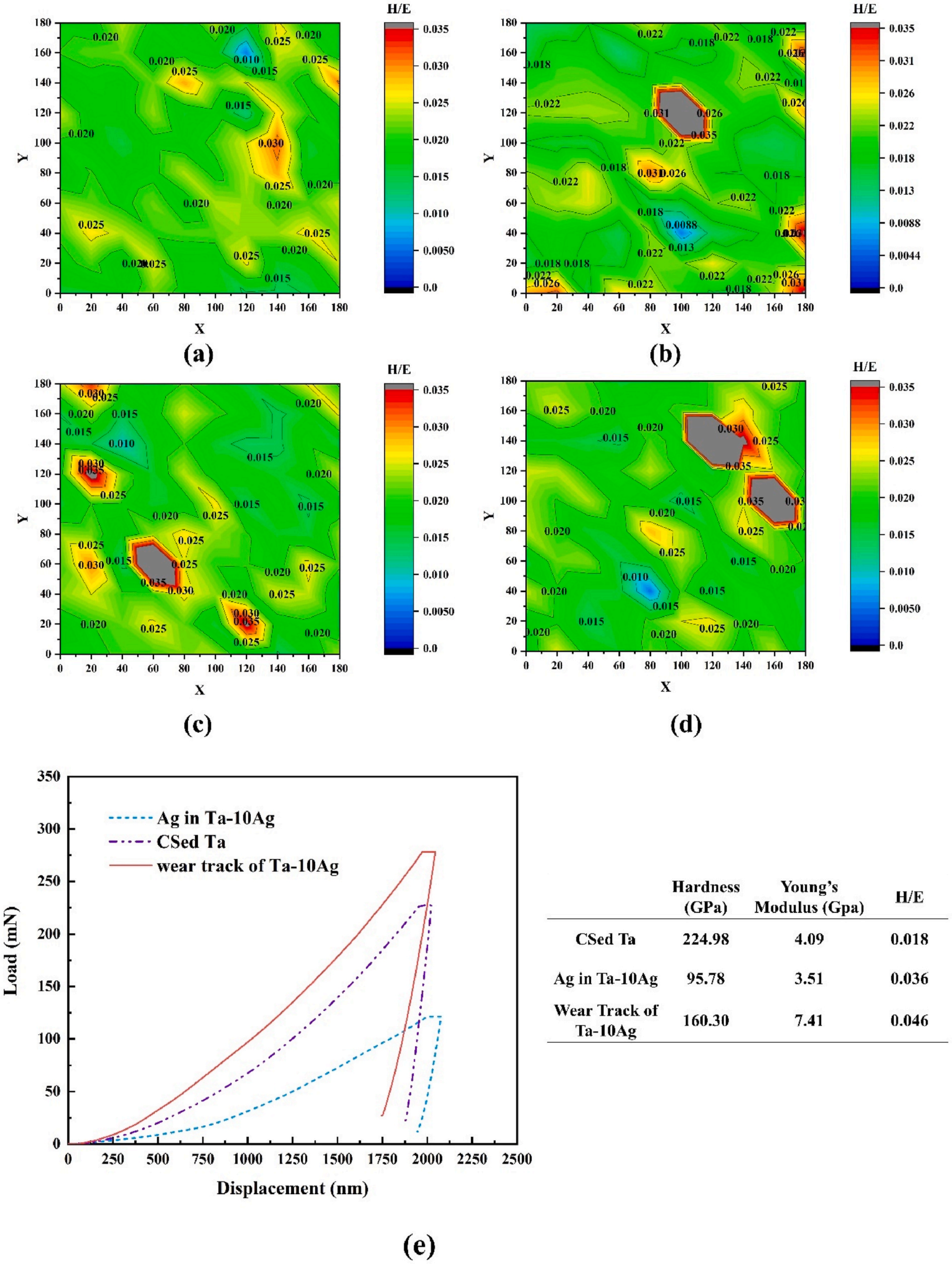

	Hardness (GPa)	Young's Modulus (Gpa)	H/E
CSed Ta	224.98	4.09	0.018
Ag in Ta-10Ag	95.78	3.51	0.036
Wear Track of Ta-10Ag	160.30	7.41	0.046

Fig. 15. (a)–(d) H/E mapping of pure Ta and Ta/Ag composites measured by nanoindentation.(e) load-unload profile of Ag agglomerations, Ta matrix and Ta–10Ag wear track observed by nanoindentation.

To analyze wear mechanisms, the hardness-to-elasticity ratio (H/E), or plasticity index, was employed [44]. Hardness reflects a material's strength, with higher hardness requiring more force for deformation. Elastic modulus determines a material's tendency to reach its yield point; materials with lower elastic modulus endure more strain before damage. Consequently, materials with higher H/E values resist plastic deformation, adhesive wear, and abrasive wear more effectively. Fig. 15 illustrates the H/E contour map of Ta and Ta/Ag coatings based on nanoindentation mapping. Pure Ta coatings exhibit relatively low H/E values (~0.02), whereas regions within Ta/Ag composites, particularly Ag agglomerations, show higher H/E values (~0.03). The elevated H/E in Ag agglomerations results from Ag's inherently low elastic modulus combined with increased hardness due to high dislocation density and grain refinement caused by severe deformation during the cold spray process.

In contrast, EBSD analysis indicates that Ta particles underwent minimal deformation, with grain refinement confined to impact interfaces. Consequently, the Ta matrix exhibited less strain hardening, retaining a high Young's modulus and lower H/E values compared to Ag agglomerations. Ta's higher modulus creates localized stresses during wear, increasing crack initiation and propagation under cyclic loading. Weak inter-particle bonding, due to the low cold-spray parameters, further facilitate crack formation. Cracks propagate rapidly, leading to material removal from deeper layers. Additionally, brittle oxide layers formed during wear crack easily, further enhancing material loss. In low-Ag coatings, such as Ta–2Ag, sparse Ag agglomerations within the Ta matrix cause severe friction load oscillations, inducing high-frequency impact loads that promote crack initiation. This results in high material removal, intense third-body abrasive wear, and the production of abundant debris particles.

Higher Ag volume fractions, as in Ta–5Ag and Ta–10Ag, reduce the coefficient of friction (COF) and mitigate friction load oscillations due to the denser Ag distribution (Fig. 1 in supplementary document). Meanwhile, Ag fill in cracks, minimizing material fatigue fracture. Moreover, post-wear nanoindentation of the Ta–10Ag wear track revealed an H/E ratio of 0.045—double that of pure cold-sprayed Ta, due to strain hardening and mechanical mixing of Ta and Ag. The increased H/E enhances resistance to fatigue and adhesive wear, shifting the dominant wear mechanism to abrasive wear via micro-cutting or micro-ploughing, resulting in narrower and shallower grooves (Fig. 14d).

Overall, the addition of Ag offers lubrication mechanism and increases the H/E ratio of wear surfaces through mechanical mixing and strain hardening. These enhancements improve the fatigue and adhesive wear resistance of cold-sprayed (CS) Ta/Ag composite coatings while reducing the formation of excessive debris particles. Consequently, this minimizes the risk of immune responses triggered by debris particles.

4. Conclusions

In this study, dense Ta/Ag MMCs were successfully cold-sprayed onto AZ31B Mg alloys. The adhesive strength, corrosion resistance, and wear properties of the coated samples were systematically assessed. The following conclusions were drawn.

1. The bonding between Ta/Ag coatings and AZ31 Mg alloys is primarily due to mechanical interlocking. Adhesive strength ranged from 22.5 to 27.5 MPa, with coating failures originating at unbonded boundaries within the coatings.
2. Ta/Ag coatings provided corrosion protection for Mg alloys in chloride environments through cathodic protection for Ta matrix by dissolving Ag agglomerations. However, unbonded Ta–Ag interfaces intensified Ag dissolution, reducing corrosion resistance as Ag content increased.
3. Higher Ag content improved fatigue wear resistance due to Ag's ductility, low friction, and high conductivity. Ag filled microcracks during wear, increasing the H/E ratio and preventing crack propagation and debris formation.
4. Ta–5Ag achieved the best balance of corrosion and wear resistance, while Ta–10Ag showed superior wear resistance but poor long-term corrosion resistance. Addressing unbonded Ta/Ag interfaces, such as through in-situ peening or multilayer structures, could further enhance protection properties In general, Cold spray exhibit promising potential to fabricate MMCs coatings to achieve medium to long-term protection for active Mg alloys.

Declaration of competing interest

The authors declare that they have no known competing financial interests or personal relationships that could have appeared to influence the work reported in this paper.

Acknowledgement

The authors are grateful for the financial support from the China Scholarship Council (No.202006220041).

Appendix A. Supplementary data

Supplementary data to this article can be found online at https://doi.org/10.1016/j.jmrt.2025.03.048.

References

[1] Radha R, Sreekanth D. Insight of magnesium alloys and composites for orthopedic implant applications–a review. J Magnesium Alloys 2017;5(3):286–312.

[2] Kamrani S, Fleck C. Biodegradable magnesium alloys as temporary orthopaedic implants: a review. Biometals 2019;32:185–93.

[3] Vormann J. Magnesium: nutrition and metabolism. Mol Aspect Med 2003;24(1–3):27–37.

[4] Chalisgaonkar R. Insight in applications, manufacturing and corrosion behaviour of magnesium and its alloys–a review. Mater Today Proc 2020;26:1060–71.

[5] Lindström R, Johansson L-G, Thompson GE, Skeldon P, Svensson J-E. Corrosion of magnesium in humid air. Corros Sci 2004;46(5):1141–58.

[6] Witte F. The history of biodegradable magnesium implants: a review. Acta Biomater 2010;6(5):1680–92.

[7] Niu J, Huang H, Pei J, Jin Z, Guan S, Yuan G. Research and development strategy for biodegradable magnesium-based vascular stents: a review. Biomaterials Translational 2021;2(3):236.

[8] Esmaily M, Svensson JE, Fajardo S, Birbilis N, Frankel GS, Virtanen S, Arrabal R, Thomas S, Johansson LG. Fundamentals and advances in magnesium alloy corrosion. Prog Mater Sci 2017;89:92–193.

[9] Xin Y, Huo K, Tao H, Tang G, Chu PK. Influence of aggressive ions on the degradation behavior of biomedical magnesium alloy in physiological environment. Acta Biomater 2008;4(6).

[10] Takenaka T, Ono T, Narazaki Y, Naka Y, Kawakami M. Improvement of corrosion resistance of magnesium metal by rare earth elements. Electrochim Acta 2007;53(1):117–21.

[11] Hornberger H, Virtanen S, Boccaccini AR. Biomedical coatings on magnesium alloys – a review. Acta Biomater 2012;8(7):2442–55.

[12] Zhao Y, Bai J, Xue F, Zeng R, Wang G, Chu PK, Chu C. Smart self-healing coatings on biomedical magnesium alloys: a review. Smart Materials in Manufacturing 2023;1:100022.

[13] Xiao Z, He T, Liu X, Dai Y, She J, Jiang Y, Qi F, Ouyang X. Influence of ferrum film by fcva deposition technique on properties of we43 magnesium alloy. J Rare Earths 2024;42(12):2332–40.

[14] Li L, Zhang Z, Zhang D, Qi F, Dai Y, Wei W, Ouyang X. Effects of metal ion implantation (fe, ti, zn and zr) on mechanical properties, corrosion resistance and biocompatibility of we43 mg alloy. J Magnesium Alloys 2025;13(1):296–310.

[15] Dorozhkin SV. Calcium orthophosphate coatings on magnesium and its biodegradable alloys. Acta Biomater 2014;10(7):2919–34.

[16] Amaravathy P, Sathyanarayanan S, Sowndarya S, Rajendran N. Bioactive ha/tio2 coating on magnesium alloy for biomedical applications. Ceram Int 2014;40(5):6617–30.

[17] Rahman M, Li Y, Wen C. Ha coating on mg alloys for biomedical applications: a review. J Magnesium Alloys 2020;8(3):929–43.

[18] Zhou W, Shan D, Han E-H, Ke W. Structure and formation mechanism of phosphate conversion coating on die-cast az91d magnesium alloy. Corros Sci 2008;50(2):329–37.

[19] Wu G, Zeng X, Yuan G. Growth and corrosion of aluminum pvd-coating on az31 magnesium alloy. Mater Lett 2008;62(28):4325–7.

[20] Durdu S, Usta M. Characterization and mechanical properties of coatings on magnesium by micro arc oxidation. Appl Surf Sci 2012;261:774–82.

[21] Hu R-G, Zhang S, Bu J-F, Lin C-J, Song G-L. Recent progress in corrosion protection of magnesium alloys by organic coatings. Prog Org Coating 2012;73(2–3):129–41.
[22] Chen Q, Thouas GA. Metallic implant biomaterials. Mater Sci Eng R Rep 2015;87: 1–57.
[23] Guo SF, Pan FS, Zhang HJ, Zhang DF, Wang JF, Miao J, Su C, Zhang C. Fe-based amorphous coating for corrosion protection of magnesium alloy. Mater Des 2016; 108:624–31.
[24] Zhang D, Wei B, Wu Z, Qi Z, Wang Z. A comparative study on the corrosion behaviour of al, ti, zr and hf metallic coatings deposited on az91d magnesium alloys. Surf Coating Technol 2016;303:94–102.
[25] Xie Z-H, Li D, Skeete Z, Sharma A, Zhong C-J. Nanocontainer-enhanced self-healing for corrosion-resistant ni coating on mg alloy. ACS applied materials & interfaces 2017;9(41):36247–60.
[26] Zhu L, Song G. Improved corrosion resistance of az91d magnesium alloy by an aluminium-alloyed coating. Surf Coating Technol 2006;200(8):2834–40.
[27] Mahon OR, Dunne A. Disease-associated particulates and joint inflammation; mechanistic insights and potential therapeutic targets. Front Immunol 2018;9: 1145.
[28] Assadi H, Kreye H, Gärtner F, Klassen T. Cold spraying – a materials perspective. Acta Mater 2016;116:382–407.
[29] Xie X, Yin S, Raoelison R-n, Chen C, Verdy C, Li W, Ji G, Ren Z, Liao H. Al matrix composites fabricated by solid-state cold spray deposition: a critical review. J Mater Sci Technol 2021;86:20–55.
[30] Huang C, List A, Wiehler L, Schulze M, Gärtner F, Klassen T. Cold spray deposition of graded al-sic composites. Addit Manuf 2022;59:103116.
[31] Kovarik O, Cizek J, Yin S, Lupoi R, Janovska M, Cech J, Capek J, Siegl J, Chraska T. Mechanical and fatigue properties of diamond-reinforced cu and al metal matrix composites prepared by cold spray. J Therm Spray Technol 2022;31(1):217–33.
[32] Tang J, Zhao Z, Liu H, Cui X, Wang J, Xiong T. A novel bioactive ta/hydroxyapatite composite coating fabricated by cold spraying. Mater Lett 2019;250:197–201.
[33] Sanpo N, Ang SM, Cheang P. Antibacterial property of cold sprayed chitosan-cu/al coating. J Therm Spray Technol 2009;18:600–8.
[34] Frattolin J, Roy R, Rajagopalan S, Walsh M, Yue S, Bertrand OF, Mongrain R. A manufacturing and annealing protocol to develop a cold-sprayed fe-316l stainless steel biodegradable stenting material. Acta Biomater 2019;99:479–94.
[35] Li W, Yang K, Zhang D, Zhou X, Guo X. Interface behavior of particles upon impacting during cold spraying of cu/ni/al mixture. Mater Des 2016;95:237–46.
[36] Wauthle R, van der Stok J, Yavari SA, Van Humbeeck J, Kruth JP, Zadpoor AA, Weinans H, Mulier M, Schrooten J. Additively manufactured porous tantalum implants. Acta Biomater 2015;14:217–25.
[37] Black J. Biologic performance of tantalum. Clin Mater 1994;16(3):167–73.
[38] Clement JL, Jarrett PS. Antibacterial silver, Metal-based drugs 1994;1(5–6): 467–82.
[39] Yu P, Perumal G, Genoud KJ, Maughan J, O'Brien FJ, Brabazon D, Xie Y, Wang J, Yin S, Lupoi R. Cold sprayed ta-ag composites: mechanistic insight into enhanced corrosion resistance and antibacterial ability. Corros Sci 2024;237:112284.
[40] Heshmati M, Seifzadeh D, Shoghi P, Gholizadeh-Gheshlaghi M. Duplex ni-zn-cu-p/ni-p electroless coating on magnesium alloy via maleic acid pretreatment. Surf Coating Technol 2017;328:20–9.
[41] Rajabalizadeh Z, Seifzadeh D. Application of electroless ni-p coating on magnesium alloy via cro3/hf free titanate pretreatment. Appl Surf Sci 2017;422:696–709.
[42] Hernández HH, Reynoso AMR, González JCT, Morán COG, Hernández JGM, Ruiz AM, Hernández JM, Cruz RO. Electrochemical impedance spectroscopy (eis): a review study of basic aspects of the corrosion mechanism applied to steels. Electrochemical impedance spectroscopy 2020:137–44.
[43] Levard C, Mitra S, Yang T, Jew AD, Badireddy AR, Lowry GV, Brown Jr GE. Effect of chloride on the dissolution rate of silver nanoparticles and toxicity to e. Coli. Environmental Science & Technology 2013;47(11):5738–45.
[44] Leyland A, Matthews A. On the significance of the h/e ratio in wear control: A nanocomposite coating approach to optimised tribological behaviour. Wear 2000; 246(1):1–11.